BINARY PARTICLE MIXTURES AS A HEAT TRANSFER MEDIA IN SHELL-AND-PLATE MOVING PACKED BED HEAT EXCHANGERS

by

Chase Ellsworth Christen

A thesis

submitted in partial fulfillment

of the requirements for the degree of

Master of Science in Mechanical Engineering

Boise State University

May 2021

BOISE STATE UNIVERSITY GRADUATE COLLEGE

DEFENSE COMMITTEE AND FINAL READING APPROVALS

of the thesis submitted by

Chase Ellsworth Christen

Thesis Title: Binary Particle Mixtures as a Heat Transfer Media in Shell-and-Plate Moving Packed Bed Heat Exchangers

Date of Final Oral Examination: 12 March 2021

The following individuals read and discussed the thesis submitted by student Chase Ellsworth Christen, and they evaluated his presentation and response to questions during the final oral examination. They found that the student passed the final oral examination.

Todd P. Otanicar, Ph.D. P.E.	Chair, Supervisory Committee
Krishna Pakala, Ph.D.	Member, Supervisory Committee
David Estrada, Ph.D.	Member, Supervisory Committee

The final reading approval of the thesis was granted by Todd P. Otanicar, Ph.D., Chair of the Supervisory Committee. The thesis was approved by the Graduate College.

ACKNOWLEDGMENTS

I would like to thank Dr. Todd Otanicar for his guidance throughout the last two years. I have grown as a person and a researcher due to him and my lab members throughout my time at Boise State University. I would also like to thank Dr. David Estrada for lending the TEMPOS Thermal Properties Analyzer probe used in this study.

ABSTRACT

Solid particles are being considered in several high temperature thermal energy storage systems and as heat transfer media in concentrated solar power (CSP) plants. The downside of such an approach is the low overall heat transfer coefficients in shell-and-plate moving packed bed heat exchangers caused by the inherently low packed bed thermal conductivity values of the low-cost solid media. Choosing the right particle size distribution of currently available solid media can make a substantial difference in packed bed thermal conductivity, and thus, a substantial difference in the overall heat transfer coefficient of shell-and-plate moving packed bed heat exchangers. Current research exclusively focuses on continuous unimodal distributions of alumina particles. The drawback of this approach is that larger particle sizes require wider particle channels to meet flowability requirements. As a result, only small particle sizes with low packed bed thermal conductivities have been considered for the use in the falling-particle Gen3 CSP concepts. Here, binary particle mixtures, which are defined in this thesis as a mixture of two continuous unimodal particle distributions leading to a continuous bimodal particle distribution, are considered to increase packed bed thermal conductivity, decrease packed bed porosity, and improve moving packed bed heat exchanger performance. This is the first study related to CSP solid particle heat transfer that has considered the packed bed thermal conductivity and moving packed bed heat exchanger performance of bimodal particle size distributions at room and elevated temperatures. Considering binary particle mixtures that meet particle sifting segregation criteria, the overall heat transfer coefficient

of shell-and-plate moving packed bed heat exchangers can be increased by 23% when compared to a monodisperse particle system. This work demonstrates that binary particle mixtures should be seriously considered to improve shell-and-plate moving packed bed heat exchangers.

TABLE OF CONTENTS

LIST OF TABLES

LIST OF FIGURES

LIST OF ABBREVIATIONS

CSP	Concentrated Solar Power
NREL	National Renewable Energy Laboratory
sCO_2	Supercritical Carbon Dioxide
SolarPACES	Solar Power and Chemical Energy Systems
ZBS	Zehner, Bauer, and Schlünder

CHAPTER ONE: INTRODUCTION

1.1 Introduction to Concentrated Solar Power

Concentrated solar power (CSP) works by increasing the radiative flux on a receiver area with the goal of heating a working fluid that can then be used to generate electricity in a power cycle. The four CSP technologies used today are parabolic troughs, linear Fresnel, parabolic dish, and power towers. Parabolic troughs and power towers are the most popular CSP systems across the world according to data collected by SolarPACES, an international program of the International Energy Agency, and the National Renewable Energy Laboratory (NREL) [1]. Table 1.1 shows the number of CSP projects currently operating, under construction, and under development for each of the four CSP technologies as of 2019 [1].

Table 1.1 CSP technology deployed across the world as of 2019 [1]**.**

CSP Technology (Concentration Ratio)	Operating	Under Construction	Under Development
Parabolic Trough (15-45)	84	12	15
Linear Fresnel (10-40)	7	4	1
Parabolic Dish (100-1000)	0	0	4
Power Towers (100-1500)	21	4	21

While parabolic troughs are the most widely deployed CSP system worldwide, parabolic troughs are limited to an operating temperature range of 100-500 °C, which limits the efficiency of the power cycles for this technology [2]. The temperature limit of parabolic troughs is due to heat loss in the system and the material limitations of the typical working fluids which include synthetic thermal oil, water/steam, and molten salt [3]. To exceed the current temperature limitations of parabolic troughs, solar power towers have gained traction in recent years. Solar power towers work by using a field of mirrors, also known as a heliostat field, that reflects light to a single point which can heat materials to well over 1000 °C. The higher temperature limit allows power towers to achieve higher thermal-to-electric conversion efficiencies and lower costs for thermal energy storage [4]. Current commercial power towers utilize either molten salts at 565 °C or superheated steam over 550 °C [5]. These operating temperatures fall well below the temperature limits that could be achieved by power towers. As a result, the Solar Energy Technology Office (SETO) started the Gen3 CSP funding program, a program that has the goal of drastically reducing the cost of power towers by integrating a high-pressure (≥ 20 MPa), high-temperature (≥ 700 °C) Brayton power cycle using supercritical carbon dioxide (sCO_2) as the working fluid [5]. To achieve the higher temperatures required for the sCO_2 power cycles, three potential heat transfer medias are being considered: 1) molten salt, 2) solid particles, and 3) gas phase [5]. Significant research has been conducted for both molten salt [6]–[8] and gas phase [9]–[11] technologies; however, this study will exclusively focus on the particle pathway.

1.2 Falling-Particle CSP

Figure 1.1 illustrates a high-level diagram of a counterflow shell-and-plate moving packed bed heat exchanger system. Reflected sunlight from the heliostat is used to heat particles in the receiver. Once heated, the particles are either put through the heat exchanger immediately, or the hot particles are stored until electricity is required [12]. The ability to store heat in packed particle beds for extended periods of time is one of the largest benefits to particle-based CSP concepts because it not only allows the system to operate smoothly in the case of a patch of overcast skies, but it also allows for the system to operate when electricity loads are highest in the evenings. Once the particles pass through the particle-to-sCO_2 heat exchanger, the particles are brought back to the top of the particle receiver to start the process again.

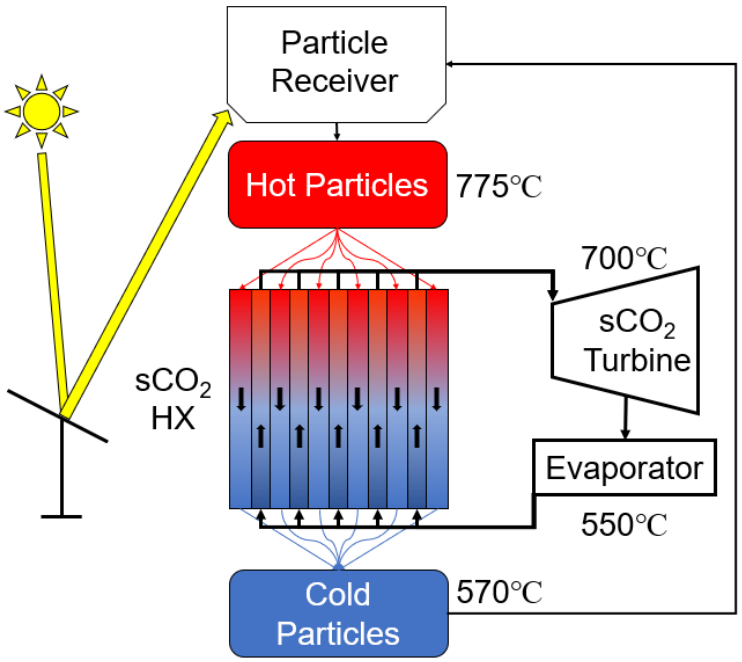

Figure 1.1 High-level shell-and-plate moving packed bed heat exchanger diagram.

Solid particles are being considered as a heat transfer media due to many advantages it has over current heat transfer fluids:

1. Proposed particles such as sand and CARBO ceramics materials are chemically inert and stable for temperatures exceeding 1000 °C.
2. Particles can easily be stored at elevated temperatures for energy storage.
3. Particles are not susceptible to freezing like molten salt.
4. Particle costs are relatively inexpensive.

While solid particles provide the aforementioned benefits, there are significant challenges in particle CSP designs including particle conveyance [13], attrition [14], and heat transport [15]–[18]. This thesis will exclusively address the heat transport problem that exists in particle-to-sCO_2 heat exchangers.

There are multiple competing particle-to-sCO_2 heat exchangers designs including fluidized beds, shell-and-tube moving packed bed heat exchangers, and shell-and-plate moving packed bed heat exchangers [15]. Fluidized beds have been shown to produce higher heat transfer coefficients than the other heat exchanger technologies (> 500 W/m^2-K) [19]–[22]; however, the cost of the fluidized heat exchanger system kept Sandia National Laboratory from building this design for their 100 kW_t particle-to-sCO_2 demonstration project [15].

Baumann and Zunft have experimentally and computationally studied shell-and-tube moving packed bed heat exchangers [23], [24]. Their results demonstrate that heat transfer coefficients of 240 W/m^2-K were achieved for particles that were heated to 500 °C and moving with a superficial bulk velocity of 5 mm/s. While the shell-and-tube heat exchanger design ranked highest in Ho et al.'s weighted ranking, the shell-and-plate

moving packed bed heat exchanger was chosen because the shell-and-plate design was believed to have the most room for performance improvement and commercialization [15].

The shell-and-plate moving packed bed heat exchanger, which will be the focus of the overall heat transfer coefficient modeling in this study, have been extensively researched by Albrecht and Ho [25]–[30]. Their research consists of numerical models and experimental measurements. Albrecht and Ho found that the particle-wall convection coefficient had an asymptote value of 200 W/m^2-K for CARBO Ceramics ID50 (~280 μm) and HSP 40/70 (~210-420 μm) in a 4 mm channel. In the same study, the mass flow rate of ID50 was studied at 600 °C in a mock heat exchanger that mimicked the design of the 100 kW$_t$ shell-and-plate moving packed bed heat exchanger prototype (6 mm 316 stainless steel plates with 6 mm spacing and a feeder angle of 77°). The particle flow at elevated temperature was shown to experience funnel flow, a particle flow profile where the center particle channels flow faster than the adjacent outside channels. The funnel flow profile was attributed to an increase in particle-wall friction at elevated temperatures. Recent work has included testing of a 100 kW$_t$ moving packed bed heat exchanger prototype at intermediate temperatures (< 500 °C). The overall heat transfer coefficient was measured to be 50-80 W/m^{2}K, which is well below the ~120 W/m^2-K expected from using their shell-and-plate moving packed bed heat exchanger model [26].

Bauman and Zunft previously studied the thermal properties of many different granular materials options for falling-particle CSP [14]; however, their study only included two particles with the volumetric mean diameters under 1000 μm: 560 μm sintered bauxite & 800 μm quartz sand (See Figure 1.2). Studying particles with diameters below 1000 μm is essential for shell-and-plate moving packed bed heat exchangers because larger particle

require wider particle channel thicknesses, which have lower overall heat transfer coefficients, to meet particle flowability requirements [25], [27]. This study expands on Bauman and Zunft's research not only by measuring the thermal conductivity of five CARBO brand ceramic particles between 100-1000 μm, but this study also explores the benefit of using a binary particle mixture to increase the packed bed thermal conductivity.

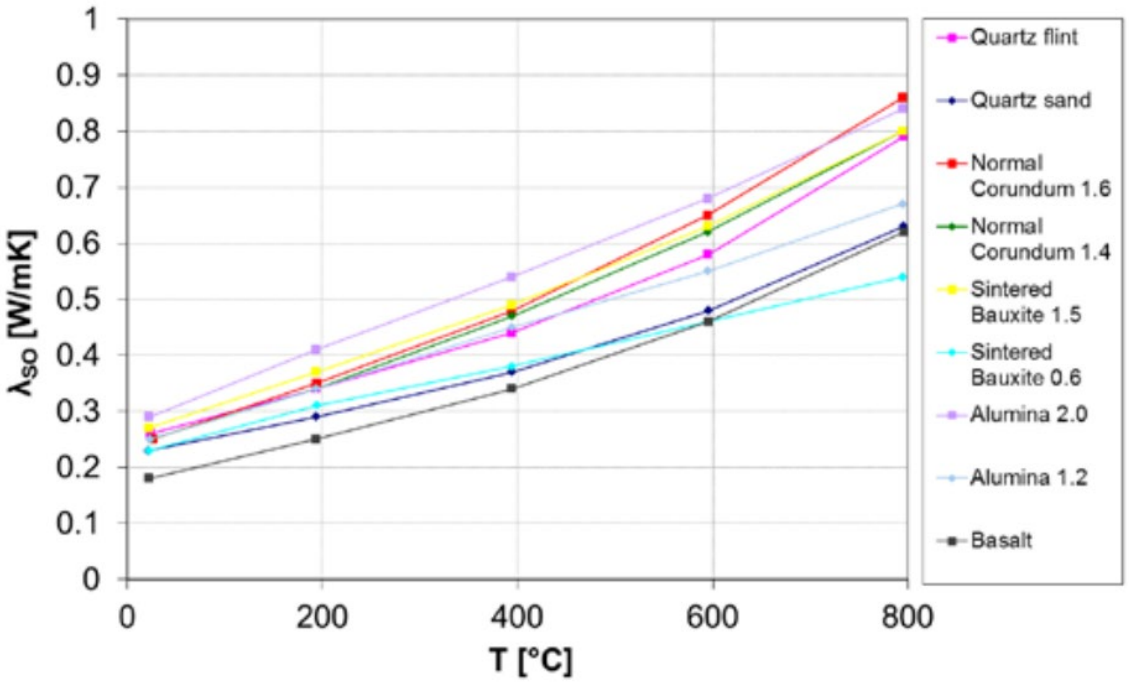

Figure 1.2 Packed bed thermal conductivity as a function of temperature for multiple particle materials. Adopted from [14].

Based on the experimental results presented, there is a need to increase packed bed thermal conductivity, while maintaining low-cost particles [14], to improve the overall heat transfer coefficient of shell-and-plate moving packed bed heat exchangers. This study proposes using binary particle mixtures, which are defined in this thesis as a mixture of two continuous unimodal particle distributions leading to a continuous bimodal particle distribution [31], to increase packed bed thermal conductivity by decreasing packed bed porosity.

The suggestion of using a binary particle mixture comes from studying the four components that change packed bed thermal conductivity according to the Zhener, Bauer, and Schlünder (ZBS) thermal conductivity model: 1) particle emissivity, 2) particle size, 3) solid particle thermal conductivity, and 4) packed bed porosity [32]. Larger particle emissivity leads to an increase in packed bed thermal conductivity; however, there would be limited improvement by focusing on emissivity because CARBO ceramic particles already have an emissivity of 0.9 [33]. Baumann and Zunft show that larger particles improve packed bed thermal conductivity at higher temperatures primarily due to an increase in radiation [14]; however, larger particle diameters require wider particle channel thicknesses to meet particle flowability requirements [25]. There will need to be more modeling and experiments before an optimal particle size distribution can be determined for moving packed bed heat exchangers. Naturally a packed bed of aluminum will have a higher thermal conductivity than a packed bed of sand, due to the higher thermal conductivity of the particle material; however, Bauman and Zunft found that choosing a particle with higher solid thermal conductivity can only marginally improve packed bed thermal conductivity [14]. Additionally, the cost of solid metal particles would be substantially higher making them impractical for CSP purposes. Finally, thermal conductivity can be increased by decreasing packed bed porosity [34]. While monodisperse particles have a relatively constant porosity for diameters larger than 100 μm [35], a significant decrease in packed bed porosity can be achieved by using a binary packed bed [36]. For this reason, exploring binary particle mixtures appears to be the most promising way to increase the packed bed thermal conductivity at little to no cost.

1.3 Research Scope and Objectives

The objective of this research is to determine whether binary particle mixtures could become a viable way of increasing the overall heat transfer coefficient for a shell-and-plate moving packed bed heat exchangers by increasing packed bed thermal conductivity through a decrease in packed bed porosity. The first step in this study is to outline the models that describe the porosity and thermal conductivity of binary particle mixtures across a range of large particle volume fractions and particle size ratios. These models are then compared with experimental measurements for 14 particle systems (5 monodisperse and 9 binary) at temperatures up to 300 °C. Once the thermal conductivity and porosity models are verified, they are utilized in a shell-and-plate moving packed bed heat exchanger model, which is used to study multiple binary mixtures of CARBOBEAD ceramic particles. The final goal is to compare the performance of monodisperse and binary particle mixtures in shell-and-plate moving packed bed heat exchangers and make recommendations for future work.

CHAPTER TWO: PACKED BED CHARACTERIZATION

2.1 Material Selection

Five CARBO ceramic particles were selected for investigation in this study: CP 16/30, CP 40/100, CP 70/140, HSP 16/30, and HSP 40/70. While sand has also been considered as a potential granular material in moving packed bed heat exchangers, the following study only considers CARBO ceramic particles due to their use in multiple previous models and experiments [25], [27], [37], [38]. CARBO ceramic particles are popular due to the availability of many sizes, relative low cost, high durability, high sphericity, and good absorptive properties.

Binary particle mixtures of CP 16/30 – CP 40/100, CP 16/30 – CP 70/140, and HSP 16/30 – HSP 40/70 were assembled with large particle volume fractions (X_L) of 0.0, 0.25, 0.50, 0.75, or 1.0. Note that when X_L is either 0.0 or 1.0, the distribution is the monodisperse particle system for the fine and coarse particle in the mixture, respectively. In total, nine binary mixtures and five monodisperse were created. The particle size distributions for the monodisperse particle systems were either provided by CARBO with the particles or found on the company‘s data sheet [39]. Particle size distributions for the binary particle mixtures were calculated by adding the coarse and fine particle size distribution multiplied by their respective particle volume fraction.

$$Q_{i,binary} = X_L Q_{i,L} + (1 - X_L) Q_{i,s} \quad (1)$$

where $Q_{i,L}$ is the volume fraction of the coarse component, $Q_{i,s}$ is the volume fraction of the fine component, and X_L is the large particle volume fraction. The particle size distribution,

particle size ratio, particle density, and Sauter mean diameter for each particle sample in this study is shown in Figure 2.1 & Table 2.1. Table A.1 in the appendix provides exact size distributions used in this study. The Sauter mean diameter, which is used in both the porosity and the thermal conductivity models, was calculated using the particle size distributions as described by Tsotsas and Schlünder for particles with the same shape and thermal conductivity [34]:

$$d_p = \left(\sum_{i=1}^{n} \frac{Q_i}{d_i} \right)^{-1} \tag{2}$$

where Q_i is the volume fraction of the particle for a given sieve size, and d_i is the mean particle diameter of a given sieve.

Table 2.1 Particles tested in this study. Particle properties can be seen in the CARBO data sheet [39]**.**

Material	Sauter Mean Diameter, d_p [µm]	Particle Density, ρ_s [g cm^{-3}]	Size Ratio, r [-]
HSP 16/30	977	3.61	N/A
HSP 40/70	297		
CP 16/30	937	3.27	N/A
CP 40/100	262		
CP 70/140	147		
HSP 16/30 – HSP 40/70, X_L = 0.25	359	3.61	0.304
HSP 16/30 – HSP 40/70, X_L = 0.50	455		
HSP 16/30 – HSP 40/70, X_L = 0.611	517		
HSP 16/30 – HSP 40/70, X_L = 0.75	621		
CP 16/30 – CP 40/100, X_L = 0.25	319	3.27	0.279
CP 16/30 – CP 40/100, X_L = 0.50	409		
CP 16/30 – CP 40/100, X_L = 0.620	473		
CP 16/30 – CP 40/100, X_L = 0.75	569		
CP 16/30 – CP 70/140, X_L = 0.25	186	3.27	0.157
CP 16/30 – CP 70/140, X_L = 0.50	254		
CP 16/30 – CP 70/140, X_L = 0.665	336		
CP 16/30 – CP 70/140, X_L = 0.75	400		

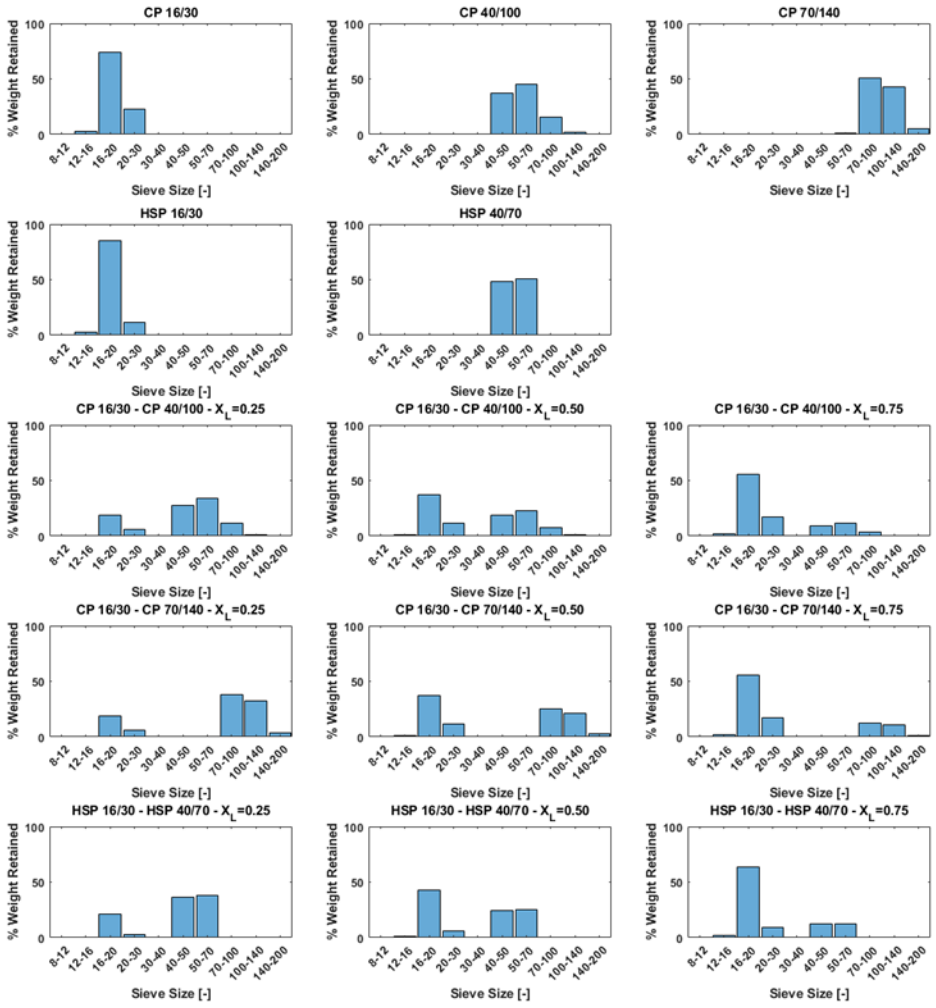

Figure 2.1 The particle size distributions for each particle sample tested. The size ratio (r) and Sauter mean diameter (dp) for each binary particle mixture is shown in the legend. Data for the particle size distributions were either provided by CARBO with the particles or taken from the company's data sheet [39].

2.2 Packed Bed Porosity

2.2.1 Porosity Measurement Methods

Because decreasing packed bed porosity was found to be the main driver in increasing the thermal conductivity of a multigranular packed beds [34], three binary particle mixtures were chosen so that a large change in porosity would be observed. It has

been shown that lower size ratios (r), the ratio of the Sauter mean diameter of the fine and coarse components (d_s/d_L), lead to a lower minimum porosity [36]. Porosity results were determined by measuring the mass of particles in a known volume. Knowing the mass, the porosity can be calculated as follows:

$$\varepsilon = 1 - \frac{m_b}{m_s} = 1 - \frac{m_b}{\rho_s \cancel{V}} \tag{3}$$

where m_b is the bulk mass recorded by the scale and m_s is the mass that would occupy the known volume V if it were non-porous. The non-porous mass can be calculated by knowing the absolute density of the particle and the volume occupied by the particles during the test. For this study, 50 ml of particles were poured into a 100 ml graduated cylinder, and the mass was taken with a Mettler Toledo XS403S scale. The mean of five porosity measurements was used as the porosity for a given particle mixture. The uncertainty in the measurements was calculated as follows:

$$U_\varepsilon = \sqrt{\left(\frac{\partial \varepsilon}{\partial m_b} U_{m_b}\right)^2 + \left(\frac{\partial \varepsilon}{\partial \cancel{V}} U_{\cancel{V}}\right)^2} \tag{4}$$

where U_{m_b} is the uncertainty in the mass measurement and $U_{\cancel{V}}$ is the ucertainty in the volume measurment. In this study, $U_{m_b} = 0.5\ mg$ and $U_{\cancel{V}} = 1\ mL$. Extra care was taken to ensure that the samples were well mixed when performing all porosity and thermal conductivity measurements.

2.2.2 Porosity Model

This study uses the empirical description of spherical particle binary mixtures developed by Yu & Standish [36]. This model shows how a conic equation can generally describe the relationship between the specific volume and the fractional solid volumes of binary mixtures. The model can be described as follows:

$$\left(\frac{V-V_1X_1}{V_2}\right)^2+2G\left(\frac{V-V_1X_1}{V_2}\right)\left(\frac{V-X_1-V_2X_2}{V_1-1}\right)+\left(\frac{V-X_1-V_2X_2}{V_1-1}\right)^2=1 \quad (5)$$

where V is the specific volume of the binary packing, V_1 & V_2 are the partial specific volumes of the particles in the mixture, X_1 and X_2 are the solid volume fractions of the coarse and fine particles, respectively, and G is a parameter that is dependent on the initial specific volumes and size ratio. Please note that $V_1=V_2=(1-\varepsilon_o)^{-1}$, $X_1=1-X_2$, and

$$V=\frac{-B+\sqrt{B^2-4AC}}{2A} \quad (6)$$

where,

$$A=\left(\frac{1}{V_2}\right)^2+\frac{2G}{V_2(V_1-1)}+\frac{1}{(V_1-1)^2} \quad (7)$$

$$B=-\frac{2V_1X_1}{(V_2)^2}+\frac{2G}{V_2(V_1-1)}(V_2X_1-V_2-X_1-V_1X_1)+\frac{2(V_2X_1-V_2-X_1)}{(V_1-1)^2} \quad (8)$$

$$C=-\left(\frac{V_1X_1}{V_2}\right)^2+\frac{2G}{V_2(V_1-1)}V_1X_1(V_2X_1-V_2-X_1)+\left(\frac{(V_2X_1-V_2-X_1)^2}{(V_1-1)^2}\right)^2-1 \quad (9)$$

G is the only unknown variable in equations 7-9. Luckily, G can be determined experimentally. Yu & Standish summarized experimental data from many binary mixture experiments and concluded that the maximum void contraction in packed bed porosity ($\Delta\varepsilon$) and large particle solid volume fraction leading to the largest porosity contraction (X_1^{max}) are functions of the initial monodisperse porosity (ε_0) and particle size ratio (r) [40]:

$$\Delta\varepsilon(r)=\begin{cases}\varepsilon_0(1-\varepsilon_0)(1-2.35r+1.35r^2) & r\le 0.741\\ 0 & r>0.741\end{cases} \quad (10)$$

$$X_1^{max}=\frac{1-r^2}{1+\varepsilon_0} \quad (11)$$

Assuming the binary mixtures experiences a maximum void contraction, the minimum specific volume of the binary mixture and the parameter G are calculated as follows:

$$V_{min} = \frac{1}{1 - \varepsilon_0 + \Delta\varepsilon(\mathrm{r})} \tag{12}$$

$$G = \frac{1 - \left(\frac{V_{min} - V_1 X_1^{max}}{V_2}\right)^2 - \left(\frac{V_{min} - V_2 - X_1^{max} + V_2 X_1^{max}}{V_1 - 1}\right)^2}{2\left(\frac{V_{min} - V_1 X_1^{max}}{V_2}\right)\left(\frac{V_{min} - V_2 - X_1^{max} + V_2 X_1^{max}}{V_1 - 1}\right)} \tag{13}$$

Once the parameter *G* is known, the specific volume of the binary mixture (Equation 6), and corresponding packed bed porosity can be calculated. Parametrically studying this model shows that lower particle size ratio will lead to a larger decrease in porosity for a given initial porosity. Similarly, a mixture with a lower initial porosity will have a lower porosity at the same size ratio as mixture with a higher initial porosity. Porosity is calculated from the specific volume as follows:

$$\varepsilon = 1 - \frac{1}{V} \tag{14}$$

2.2.3 Porosity Experimental Results

Figure 2.2A shows how large particle volume fraction changes the mixture composition for HSP 16/30 – HSP 40/70. The difference between near-wall packing of the coarse HSP 16/30 and the fine HSP 40/70 is evident. While HSP 40/70 appears to have the best contact with the near-wall, there is reason to believe that using a mixture of coarse and fine particles could improve heat transfer by increasing bulk thermal conductivity while also keeping near-wall contact resistance low [41].

Figure 2.2B shows the theoretical Yu & Standish porosity as a function of large particle volume fraction for each of the binary particle mixtures tested in this study. The porosity for each particle mixture initially experiences a decrease in porosity as the large particle volume fraction increases until reaching a minimum porosity value where the porosity then increases to that of a monodisperse particle system.

Figure 2.2C shows the experimental porosity results for CP 16/30 – CP 70/140 in comparison to the theoretical model. As expected, the mixture experiences a decrease in porosity from the introduction of a binary particle mixture; however, the decrease in porosity is not as pronounced as expected. There a few explanations for the deviation in the results. First, the particle distributions are not strictly binary, instead the distributions are bimodal. This thesis approximates each CARBO particle system (e.g. HSP 16/30) as a monodisperse particle with the Sauter mean diameter calculated from each particle distribution. This could impact the porosity measurements; however, the size distribution for each CARBO particle is narrow, so the impact of this on the measurement should be minor. Secondly, due to the complexity of real-life particle packing, it is very difficult to create a model that accurately captures all packing mechanisms. Theoretical correlations for particle packing have been known to overestimate the contraction in porosity, especially when $0.5 < X_L < 0.75$ [42], [43]. For all of the binary particle mixtures studied (see Figure 2.3), there is consistently higher error when X_L=0.5 & X_L=0.75. Table B.1 in the appendix shows that when measurements are outside $0.5 < X_L < 0.75$, the difference between the measurements and model is less than 10%. As a result, this porosity model will be used in this study for the packed bed thermal conductivity model.

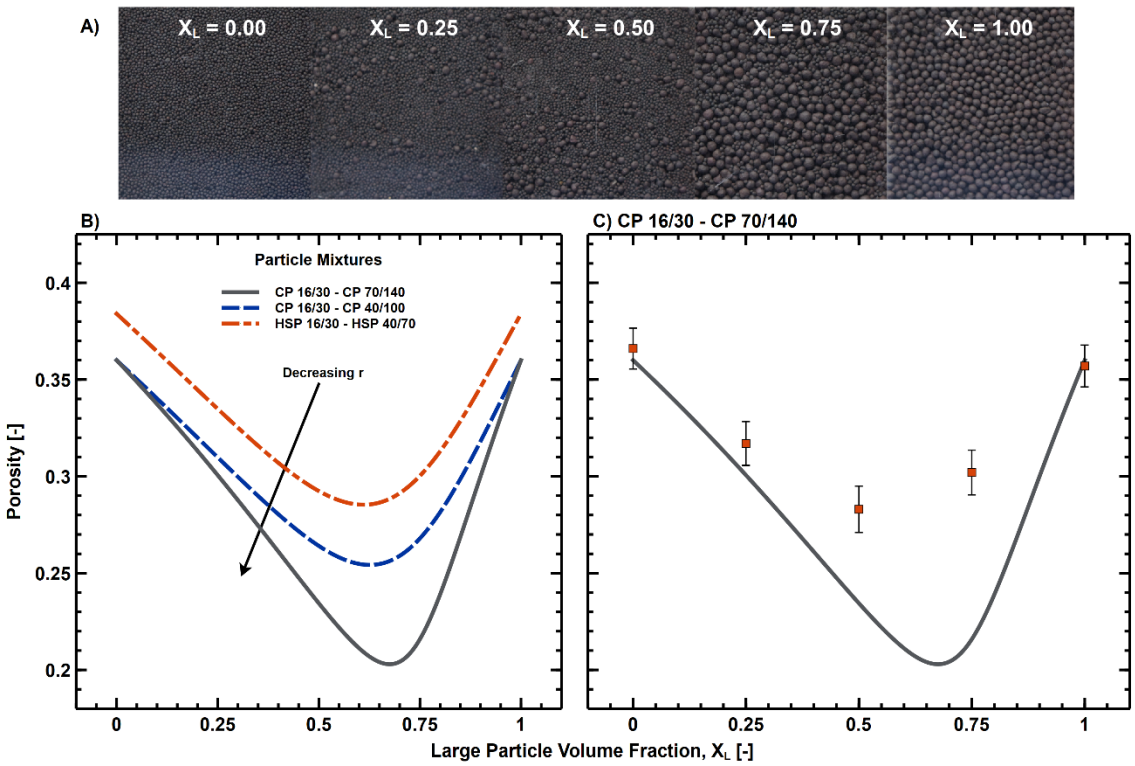

Figure 2.2 A) Particle mixtures of HSP 16/30 - HSP 40/70 used in this study. Each image is approximately 20mm x 20mm. B) Theoretical porosity as a function on large particle volume fraction for each of the binary particle mixtures tested. C) Porosity as a function of large particle volume fraction for CP 16/30 – CP 70/140. The square markers are the porosity measurements taken at each large particle volume fraction. Error bars were calculated using propogation of error (See Equation 4).

While bulk porosity for a stagnant packed bed is shown to decrease in the following thesis, more work should be done to show that the moving packed bed porosity is decreased. Because smaller particles have been shown in multiple studies to be the biggest factor in increasing the overall heat transfer coefficient [25], [41], [44], it will be important to study if a decrease in bulk and near-wall porosity from using a particle size distribution can outperform current single particle systems.

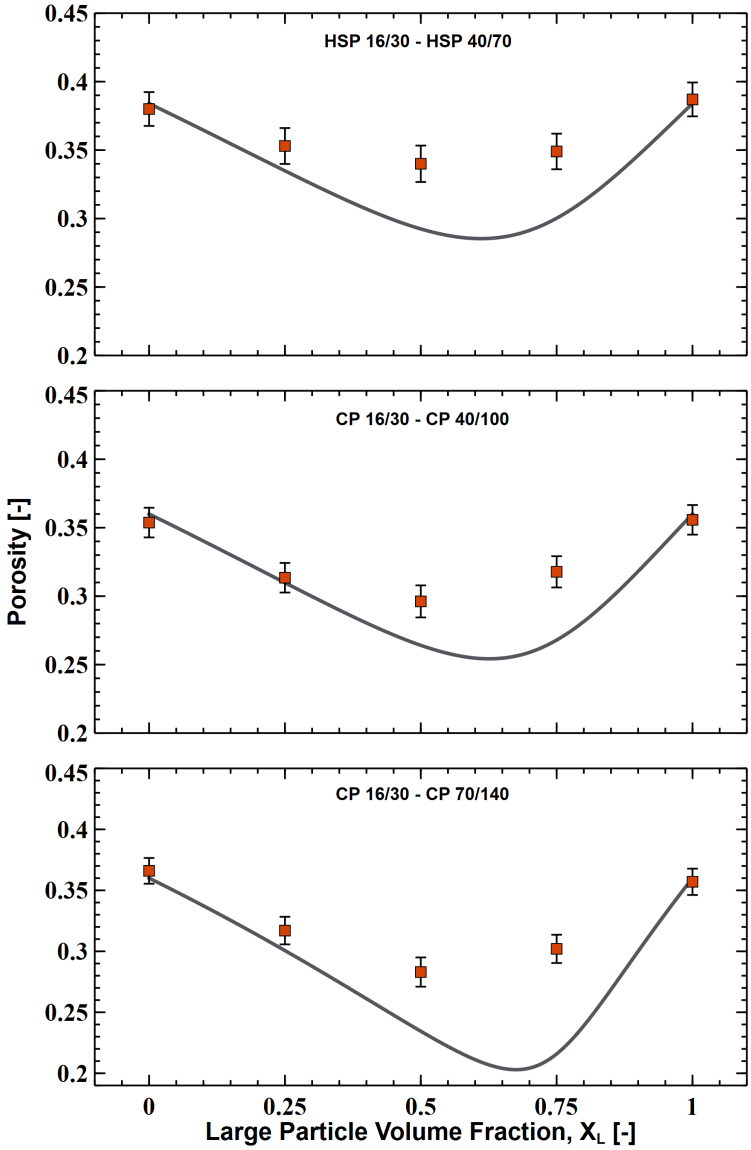

Figure 2.3 Comparison between the porosity model (grey solid line) and experimental measurements (orange squares). Error bars were calculated using propogation of error (See Equation 4).

2.3 Packed Bed Effective Thermal Conductivity

2.3.1 Thermal Conductivity Measurement Methods

The TEMPOS Thermal Properties Analyzer, a hand-held needle probe that uses a transient line heat source method to measure the thermal conductivity, was used for all the monodisperse and binary particle distributions at temperatures 25, 100, and 150 °C. To make a measurement, the probe was inserted into a 2” x 2” x 4 ½” container of the particles

being tested. The dimensions of the container were determined to ensure that at least 1.5 cm of material was parallel to the probe on all sides as per the recommendations of the user manual. The mean of ten measurements at each temperature is presented as the packed bed thermal conductivity. An uncertainty of ±10% is applied as the uncertainty as stated by the TEMPOS Thermal Analyzer user manual.

Because the TEMPOS Thermal Analyzer is limited to measuring thermal conductivity up to temperatures of 150 °C, two particles samples were sent to Thermtest, a company that specializes in building thermal conductivity instrumentation and taking thermal conductivity measurements. The particle samples that were sent to Thermtest were CP 16/30 and the binary mixture CP 16/30 – CP 70/140 X_L=0.5. These samples were tested at temperatures of 100, 250, and 300 °C on the Thermtest Hot Disk TPS 2500 S, an instrument that uses a transient plane source (TPS) hot disk method in accordance with ISO22007-2.2. An uncertainty of ±5% is applied as the uncertainty as stated by the TPS user manual.

2.3.2 Yagi & Kuni Model

The Yagi & Kuni packed bed thermal conductivity model [45] has been used by Albrecht & Ho [26], [46] as well as Yin et al. [38] in moving packed bed heat exchanger modeling. Albrecht and Ho used the Yagi & Kuni model without radiation:

$$k_{s,eff} = \frac{k_g \beta (1-\varepsilon)}{\gamma \frac{k_g}{k_s} + \varphi} \tag{15}$$

where k_g is the thermal conductivity of the air, k_s is the solid particle thermal conductivity, ε is the packed bed porosity, and γ & β are constants set to 1 in this model. φ is defined by Botterill and Denloye [47]:

$$\varphi = \frac{1}{4}\left(\frac{\left(\frac{K-1}{K}\right)^2}{\ln(K) - \frac{K-1}{K}}\right) - \frac{1}{3K} \tag{16}$$

This model works well at measuring packed bed thermal conductivity at temperatures where radiation is not significant. To address radiation, Yin et al. used the Yagi & Kuni model with radiation [45]:

$$k_{s,eff} = \frac{k_g \beta(1-\varepsilon)}{\gamma \frac{k_g}{k_s} + \frac{1}{\left(\frac{1}{\varphi}\right) + \left(\frac{d_p h_{rs}}{k_g}\right)}} + \varepsilon\beta \frac{d_p h_{rv}}{k_g} \tag{17}$$

where d_p is particle diameter, h_{rs} the heat transfer coefficient of thermal radiation from particle to particle surface, and h_{rv} is the heat transfer coefficient of thermal radiation from void to void. These coefficients are as follows:

$$h_{rs} = 0.1952\left(\frac{\varepsilon_r}{2-\varepsilon_r}\right)\left(\frac{T_s}{100}\right)^3 \tag{18}$$

$$h_{rs} = \frac{0.1952}{1 + \left(\frac{\varepsilon}{2(1-\varepsilon)}\right)\left(\frac{1-\varepsilon_r}{\varepsilon_r}\right)} \left(\frac{T_s}{100}\right)^3 \tag{19}$$

where ε_r is the solid particle emissivity and T_s is the solid particle temperature in Kelvin. While this model considers radiation, the Zehner, Bauer, and Schlünder model described next will be used in this study because it is widely respected model that has been used in numerous studies in and outside of CSP research.

2.3.3 Zhener, Bauer, and Schlünder Model

The Zehner, Bauer, and Schlünder Model (ZBS Model) is used in this thesis to calculate the effective packed bed thermal conductivity [32]. The ZBS model is a well respected effective bulk thermal conductivity model that has been used in numerous studies

[14], [25], [48]–[50]. Current shell-and-plate moving packed bed heat exchanger literature applies the ZBS Model with monodisperse particles at a constant porosity [15], [25]. While this approach is great for understanding trends associated with particle size, this thesis will explore how monodisperse and binary particle systems with size distributions change packed bed porosity and effective thermal conductivity. According to Tsotsas & Schlünder, there is precedent for using the ZBS model with a wide particle size distribution as long as the Sauter mean diameter (Equation 2) and the actual packed bed porosity are used in the calculations [34]. The ZBS model is dependent on many different parameters including packed bed porosity (ε), packed bed temperature (T), Sauter mean diameter (d_p), particle emissivity (ε_r), an empirical particle contact parameter (φ), the solid particle thermal conductivity (k_s), gas thermal conductivity (k_f), and gas pressure (P).

Table 2.2 outlines all the parameters and associated references that were used in this study. The initial porosity of the five non-binary particle systems was calculated by averaging the porosity measurements for the two particle types used in this study. The average porosity of the CP and HSP particle systems were 0.36 & 0.384, respectively. These initial porosity values are acceptable for this study because they fall between the accepted porosity values for loose and dense packed spheres of 0.40 and 0.36, respectively [51].

Table 2.2 The specific assumptions made while using the ZBS model.

Parameter	Value	Units	Ref.
Sauter Mean Diameter (d_p)	See Table 1	μm	-
Initial Porosity for CP & HSP particle systems (ε_0)	0.36 & 0.384	-	Experimental Measurements
Particle Emissivity (ε_r)	0.9	-	[33]
Empirical Particle Contact (φ)	0.01	-	[52]
Particle Thermal Conductivity (k_s)	2.0	W/m-K	[15]
Gas Thermal Conductivity (k_f)	Air(T)	W/m-K	[53]
Pressure (P)	101.325	kPa	-

The equations describing the ZBS model were reproduced from a review of packed bed thermal conductivity correlations [52]. The effective thermal conductivity of the packed bed is described as follows:

$$\frac{k_{s,eff}}{k_f} = \left(1-\sqrt{1-\varepsilon}\right)\varepsilon\left[\left(\varepsilon - 1 + \frac{1}{\kappa_G}\right)^{-1} + \kappa_r\right] + \sqrt{1-\varepsilon}\left[\varphi\kappa + (1-\varphi)k_c\right] \qquad (20)$$

where

$$k_c = \frac{2}{N}\left\{\begin{array}{r} \frac{B(\kappa+\kappa_r-1)}{N^2\kappa_G\kappa}\ln\left(\frac{\kappa+\kappa_r}{B[\kappa_G+(1-\kappa_G)(\kappa+\kappa_r)]}\right) \\ +\frac{B+1}{2B}\left[\frac{\kappa_r}{\kappa_G} - B\left(1+\frac{1-\kappa_G}{\kappa_G}\kappa_r\right)\right] - \frac{B-1}{N\kappa_G} \end{array}\right\} \qquad (21)$$

and

$$N = \frac{1}{\kappa_G}\left(1+\frac{\kappa_r - B\kappa_G}{\kappa}\right) - B\left(\frac{1}{\kappa_G}-1\right)\left(1+\frac{\kappa_r}{\kappa}\right) \qquad (22)$$

The variables used in equation 20 – equation 22 are as follows:

B Empirical Deformation Parameter (~)

k_c Contact Conduction term
N Parameter (~)
ε Porosity or void fraction (~)
κ Dimensionless parameter $\equiv k_s/k_f$
κ_G Gas conduction ratio in the Knudsen regime parameter
κ_r Radiation ratio parameter $\equiv \frac{k_e^r}{k_f}$
φ Contact area fraction (~)

The deformation parameter determined by Hso et al. is used in this study because it was found to be more accurate than the original deformation parameter proposed in the ZBS model [54].

$$B = 1.364\left(\frac{1-\varepsilon}{\varepsilon}\right)^{1.055} \tag{23}$$

The radiation ratio parameter as

$$\kappa_r = \frac{k_e^r}{k_f} = \frac{4\sigma}{\left(\frac{2}{\varepsilon_r}-1\right)}T^3\frac{d_p}{k_f} \tag{24}$$

where σ is the Stefan-Boltzman Constant, ε_r is the particles emissivity, T is the temperature in Kelvin, d_p is the Sauter mean diameter, and k_f is the thermal conductivity of the fluid or gas phase. The equivalent thermal conductivity between the surfaces of the solid phase due to the Smoluchowski effect is described by the following equation:

$$\kappa_G = \frac{k_G}{k_f} = \left[1+\left(\frac{l}{d_p}\right)\right]^{-1} \tag{25}$$

where l is the mean free path, and d_p is the Sauter mean diameter. The mean free path is modified compared with the original ZBS model and is described by the following equation:

$$l = \frac{2-a_T}{a_T}\left(\frac{2\pi\tilde{R}T}{M_g}\right)^{\frac{1}{2}}\frac{k_f}{P\left(2C_p-\frac{\tilde{R}}{M_g}\right)} \tag{26}$$

where a_T is the thermal accommodation coefficient, P is the gas pressure, $\tilde{R}$ is the universal gas constant, M_g is the molecular mass of the gas, k_f is the thermal conductivity of the fluid or gas phase, T is the gas temperature, and C_p is the specific heat at constant pressure. The thermal accommodation coefficient used in this thesis was developed by Song and Yovanovich for engineering surfaces as described by the following equation [55]:

$$a_T = \exp[-0.57\left(\frac{T_x - T =_0}{T_0}\right)\left(\frac{M^*}{6.8 + M^*}\right) + \frac{2.4\mu}{(1+\mu)^2}\left\{1 - \exp\left[-0.57\left(\frac{T_s - T_0}{T_0}\right)\right]\right\} \quad (27)$$

where,

$$M^* = \begin{cases} M_g & for\ monoatomic\ gases \\ 1.4M_g & for\ diatomic/polyatomic\ gases \end{cases} \quad (28)$$

2.3.4 Thermal Conductivity Experimental Results

Figure 2.4A shows the porosity and packed thermal conductivity @ 100 °C for each of the binary particle mixtures. The models show that smaller particle size ratios lead to a lower minimum porosity and higher maximum packed bed thermal conductivity. The ZBS model is compared with experimental results for CP 16/30 - CP 70/140 at 100, 250, and 300 °C in Figure 2.4B – Figure 2.4D, respectively. Both the TEMPOS Thermal Analyzer (orange squares) and the Thermtest Hot Disk TPS 2500 S (blue circles) show good agreement with the model across the temperature range tested. Figure 2.5 shows the thermal conductivity results for each of the particle mixture tested up to 150 °C. All measurments at 25 °C were below the model; however, as the temperature increased to 150 °C, the difference between the model and measurements decreased. It is clear that the binary mixture can significantly increase the effective packed bed thermal conductivity. Raw experimental data, model calculations, and the percent difference for each measurement is shown in Table B.2 – Table B.4, which can be found in the appendix.

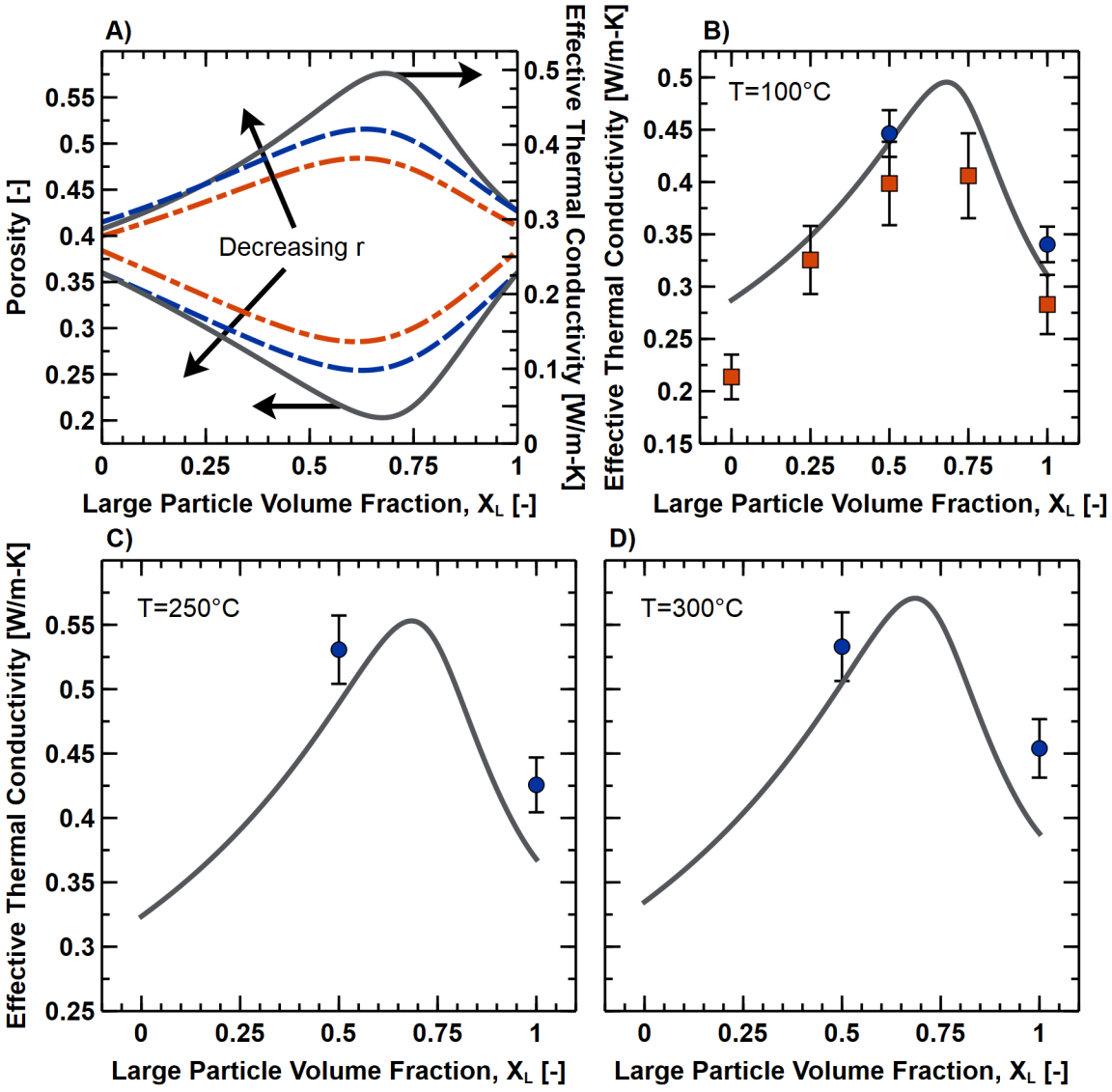

Figure 2.4 A) Theoretical Yu & Standish porosity (left axis) and ZBS thermal conductivity @ 100 °C (right axis) modeled as a function of large particle volume fraction for the binary particle mixtures CP 16/30 – CP 70/140 (grey solid line), CP 16/30 – CP 40/100 (blue dashed line), and HSP 16/30 – HSP 40/70 (orange dot-dashed). B-D) Effective thermal conductivity experimental results for CP 16/30 – CP 70/140 compared with the theoretical model at temperatures of 100, 250, and 300 °C, respectively. Error bars are a result of the uncertainty in the measurement equipment. Orange Squares – TEMPOS; Blue Circles – Thermtest.

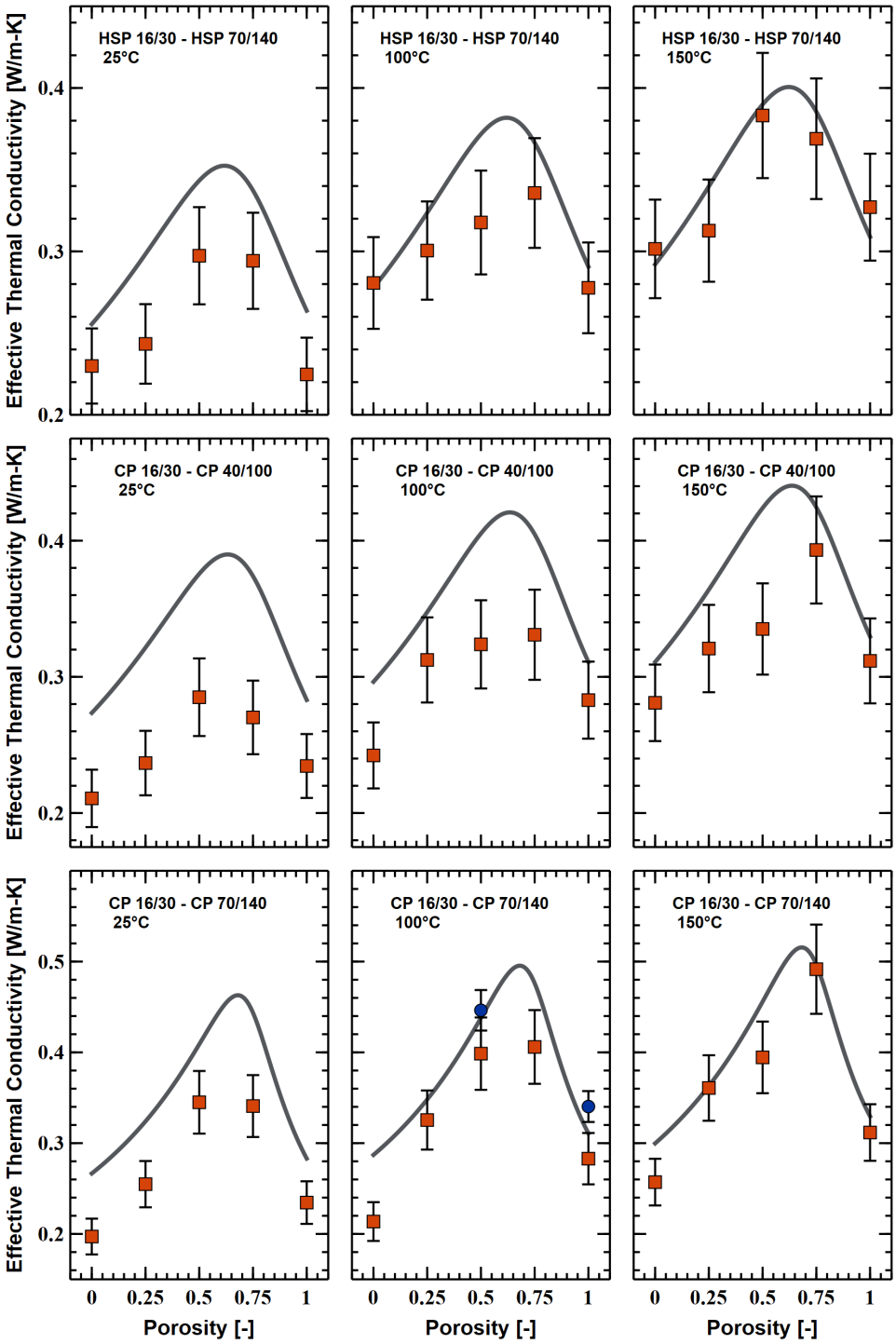

Figure 2.5 Thermal conductivity results compared to the ZBS model for each particle mixture at temperatures 25, 100, and 150 °C. Error bars are a result of the uncertainty in the measurement equipment. Orange Squares – TEMPOS; Blue Circles – Thermtest.

Because the ZBS model shows good agreement with the binary mixture effective thermal conductivity measurements taken up to 300 °C, it is appropriate to model what improvements could be made to bulk thermal conductivity at CSP operating temperatures. Figure 2.6A plots the ratio of the thermal conductivity of each of the particle mixtures to the thermal conductivity of the large particle of the binary mixture against temperature for CP 16/30 – CP 70/140. The goal of Figure 2.6A is to see if the binary mixture has a higher effective thermal conductivity than a monodisperse particle system over the proposed CSP operating temperatures (570-775 °C) [15]. In addition to the large particle volume fractions tested in this study, the binary mixture with the optimal large particle volume fraction (X_1^{max}) was added to determine the maximum possible increase in packed bed thermal conductivity. The model shows CP 16/30 – CP 70/140 X_L = 0.675 has a thermal conductivity that is 15.9 - 29% higher than CP 16/30 alone. When the same analysis is done on the other two binary particle mixtures with larger particle size ratios, the increase in thermal conductivity across the CSP operating temperatures decreases. Figure 2.6B shows the maximum increase in thermal conductivity that each of the binary mixtures in the study could achieve across CSP operating temperatures. The increase in thermal conductivity is lower for binary particle systems at higher temperatures because surface radiation becomes the largest contributor to packed bed thermal conductivity [14], [25].

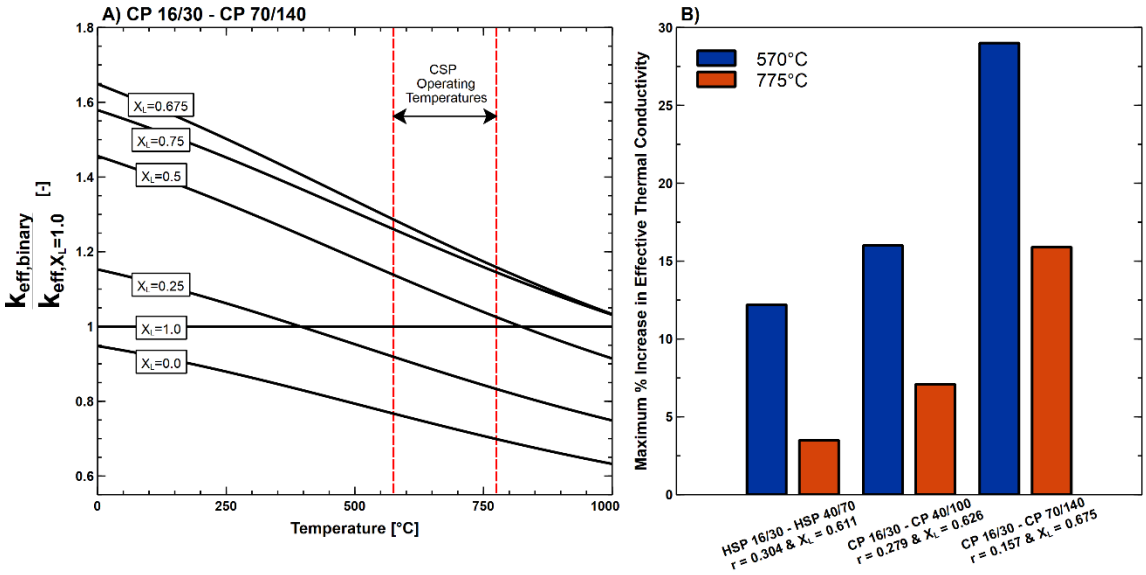

Figure 2.6 A) The thermal conductivity ratio of the binary mixture to the large particle from 0-1000 °C for CP 16/30 – CP 70/140. B) Potential increase in packed bed thermal conductivity for each of the binary particle mixtures between the proposed CSP operating temperatures.

CHAPTER THREE: MOVING PACKED BED HEAT EXCHANGER MODEL

3.1 Model Description & Diagram

3.1.1 Previous Work

There have been many experiments and models developed to understand solid particles as a heat transfer media. Both Patton et al. [18] and Golob [44] researched the convective heat transfer performance of granular materials on flat plates. Both authors found that granular media heat transfer was highly dependent on particle size, where smaller particles had higher convection coefficients.

Falcioni modeled a cylindrical moving packed bed of nickel pellets using two methods: 1) using the energy equations for the solid and fluid phase, and 2) using a non-dimensional one-equation model. Both models were found to work well at modeling the transient thermal response of the moving packed bed of nickel pellets [56].

Albrecht & Ho developed a counterflow shell-and-plate moving packed bed model which couples a 1-D sCO_2 steady-state conservation of energy equation with a 2-D steady-state conservation of energy equation for solid particles [25], [26]. The model considers the average particle-wall convection coefficient ($\bar{h}_{sw}$), the particle-wall contact resistance ($R_c^{"}$), the sCO_2 convection coefficient ($\bar{h}_{CO_2}$), and the divider wall conduction resistance $\left(\frac{t_w}{k_w}\right)$ to determine the overall heat transfer coefficient:

$$U = \left(\frac{1}{\bar{h}_{sw}} + \frac{t_w}{k_w} + R_c^{"} + \frac{1}{\bar{h}_{CO_2}}\right)^{-1} \tag{29}$$

The overall heat transfer coefficient is used to calculate the total heat transfer of the moving packed bed heat exchanger:

$$\mathrm{Q} = UA \cdot \Delta T_{lm} \tag{30}$$

where A is the surface area of the heat exchanger and ΔT_{lm} is the log mean temperature difference for a counterflow heat exchanger:

$$\Delta T_{lm} = \frac{\left(T_{s,out} - T_{CO_2,in}\right) - \left(T_{s,in} - T_{CO_2,out}\right)}{\ln\left(\frac{T_{s,out} - T_{CO_2,in}}{T_{s,in} - T_{CO_2,out}}\right)} \tag{31}$$

where $T_{s,out}$ is the particle outlet temperature, $T_{s,in}$ is the particle inlet temperature, $T_{CO_2,out}$ is the sCO_2 outlet temperature, and $T_{CO_2,in}$ is the sCO_2 inlet temperature. The log mean temperature difference is utilized because the particle and sCO_2 temperatures vary greatly across the length of the moving packed bed heat exchanger [53]. The moving bed heat exchanger model also considers multiple heat exchanger banks, major sCO_2 pressure drop, and the dependence of overall heat transfer coefficient on particle channel thickness. The most recent Albrecht & Ho moving packed bed heat exchanger model that uses the ZBS thermal conductivity model is the basis for the heat exchanger modeling in this thesis and will be described in an upcoming section [25].

Yin et al. have developed a modified version of Albrecht and Ho's original moving packed bed heat exchanger model [26] by introducing the Yagi & Kuni thermal conductivity model with radiation (see Equation 17) and using short- and long-range thermal radiation coefficients in the calculation of the particle-wall contact resistance term [38].

3.1.2 Heat Exchanger Dimensions and Material Properties

Figure 3.1 illustrates the counter-flow moving packed bed heat exchanger, and Table 3.1 shows the channel dimensions and constant material properties used in this study. The assumptions for the moving packed bed heat exchanger model, which are taken from Albrecht & Ho [25], will now be presented.

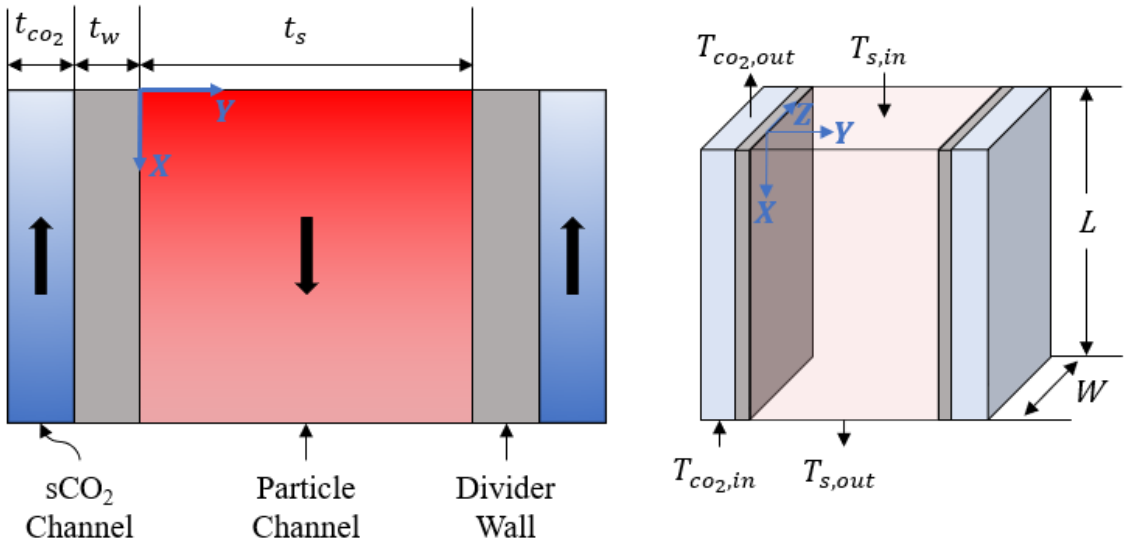

Figure 3.1 Illustration of the shell-and-plate moving packed bed heat exchanger.

Particle and sCO_2 mass flow rates are assumed to be constant and are determined using the conservation of energy:

$$\dot{Q}_{HX} = \dot{m}_s c_{p,s}(T_{s,in} - T_{s,out}) \tag{32}$$

$$\dot{Q}_{HX} = \dot{m}_{CO_2}\left[h_{CO_2}(T_{CO_2,in}, P_{CO_2}) - h_{CO_2}(T_{CO_2,out}, P_{CO_2})\right] \tag{33}$$

where h_{CO_2} is the enthalpy of the sCO_2. This study only considers a single heat exchanger bank and does not include sCO_2 pressure drop, which is considered appropriate because the pressure drop across a single bank has only a minor impact on the sCO_2 properties. Other assumptions include that the particles and air are in equilibrium [56], [57], there is only particle conduction across the y-direction, sCO_2 temperature only varies along the x-

axis because the sCO_2 convection coefficient is well established [25], and there is no heat source or sink in the moving packed bed heat exchanger.

Table 3.1 Properties for the moving packed bed heat exchanger simulation.

Property	Symbol	Value	Units	Ref.
sCO_2 Pressure	P_{CO_2}	25	MPa	[58]
sCO_2 Properties	$\mu_{CO_2}, c_{p,CO_2}, k_{CO_2}, \rho_{CO_2}$	-	-	[59], [60]
Particle Specific Heat	$c_{p,s}$	1200	J/kg-K	[26]
Particle Thermal Conductivity	k_s	2.0	W/m-K	[26]
Particle Density (CP/HSP)	ρ_s	3270/3610	kg/m^3	[39]
Particle Emissivity	ε_r	0.9	-	[33]
HX Length	L	1.0	m	
HX Width	W	0.5	m	
HX wall thickness	t_w	1.0	mm	
HX wall thermal conductivity	k_w	23	W/m-K	[26]
sCO2 channel thickness	t_{CO_2}	0.5	mm	
Particle channel thickness	t_s	6.0	mm	

3.2 Shell-and-Plate Moving Packed Bed Heat Exchanger Model

3.2.1 Governing Equations

The 1-D steady-state conservation of energy equation for the sCO_2 and the 2-D steady-state conservation of energy equation for the particles are as follows [46]:

$$\rho_{CO_2} v_{CO_2} c_{p,CO_2} \frac{dT_{CO_2}}{dx} = \frac{2q''}{t_{CO_2}} \tag{34}$$

$$\rho_s v_s c_{p,s} \frac{dT_s}{dx} = \frac{\partial}{\partial y}\left(k_{s,eff} \frac{\partial T_s}{\partial y}\right) \tag{35}$$

The two conservation equations are coupled together through the heat flux between the particle and sCO_2:

$$q''(x) = k_{s,eff} \left.\frac{dT_s}{dy}\right|_{0.x} = \frac{1}{R''(x)}\left(T_s(0,x) - T_{CO_2}(x)\right) \tag{36}$$

where *R"* is the specific thermal resistance due to the average particle-wall convection coefficient ($\bar{h}_{sw}$), the particle-wall contact resistance ($R_c^{"}$), the sCO_2 convection coefficient ($\bar{h}_{CO_2}$), and the divider wall conduction resistance $\left(\frac{t_w}{k_w}\right)$.

$$R" = \left(\frac{1}{\bar{h}_{sw}} + \frac{t_w}{k_w} + R_c^{"} + \frac{1}{\bar{h}_{CO_2}}\right) \tag{37}$$

Each component of the specific thermal resistance will be discussed in the 3.3 Overall Heat Transfer Coefficient Sensitivity section of this thesis.

Equation 35 is discretized in the y-direction so that the system of equations can be represented as a set of ordinary differential equations that can be solved using MATLAB's ode15s. In this study, the second partial derivative in the particle conservation of energy equation was discretized using second order central differencing. The boundary conditions, which occur at the first layer of particles and halfway through the particle channel (due to symmetry), are represented as follows:

$$\left.\frac{dT_s}{dy}\right|_{0.x} = \frac{2q"}{v_s\rho_s c_{p,s}\Delta y} - \frac{2k_{s,eff}\left(T_s(0,x) - T_s(1,x)\right)}{v_s\rho_s c_{p,s}(\Delta y)^2} \tag{38}$$

$$\left.\frac{dT_s}{dy}\right|_{\frac{t_s}{2}.x} = 0 \tag{39}$$

A shooting method is used to continuously update the solid mass flow rate until the simulation reaches the following boundary conditions within 0.01 °C:

$$T_{CO_2}(0) = T_{CO_2,in} = 700\ °C \tag{40}$$

$$T_{CO_2}(H) = T_{CO_2,out} = 550\ °C \tag{41}$$

$$T_s(0,y) = T_{s,in} = 775\ °C \tag{42}$$

$$\frac{1}{t_s}\int_0^{t_s} T_s(H,y)dy = T_{s,out} = 570\ °C \tag{43}$$

3.3 Overall Heat Transfer Coefficient Sensitivity

To understand why an increase in packed bed thermal conductivity could improve heat exchanger performance, the terms of the overall heat transfer coefficient (U) must be understood. The proceeding sections cover each component of the overall heat transfer coefficient (See Equation 29). The divider wall conductive resistance will not be included in the sensitivity study because the divider wall thermal conductivity is considered constant in this study. Additionally, the conductive resistance from the dividing wall is < 1% of the total resistance in the system, so it is appropriate to forgo a sensitivity study.

3.3.1 sCO_2 Convection Coefficient

The sCO_2 convection coefficient follows the Gnielinski correlation [61]:

$$h_{CO_2} = \frac{Nu_{D_h} k_{CO_2}}{D_{h,CO_2}} = \frac{k_{CO_2} 0.0214(Re^{0.8} - 100)Pr^{0.4}\left[1 + \left(\frac{D_{h,CO_2}}{L}\right)^{\frac{2}{3}}\right]\left(\frac{T_m}{T_w}\right)^{0.48}}{D_{h,CO_2}} \quad (44)$$

where D_{h,CO_2} is the hydraulic diameter of the sCO_2 channel ($D_{h,CO_2} = \frac{4t_{CO_2}W}{2(t_{CO_2}+W)} \approx 2t_{CO_2}\ for\ W \gg t_{CO_2}$), Re is the Reynolds number ($Re = \frac{v_{CO_2} D_{h,CO_2} \rho_{CO_2}}{\mu_{CO_2}}$), Pr is the Prandtl number ($Pr = \frac{\mu_{CO_2} c_{p,CO_2}}{k_{CO_2}}$), k_{CO_2} is the thermal conductivity of the sCO_2, L is the length of the heat exchanger, T_m is the mean temperature of the sCO_2, and T_w is the wall temperature. In this study, the heat exchanger is considered isobaric at 25 MPa, all sCO_2 properties are evaluated at the average sCO_2 temperature of 625 °C using the correlations from Span [60] and Vesovic [59], and the average wall temperature is 618 °C. Given the set boundary conditions of this problem, terms such as k_{CO_2}, T_m, T_w, and Pr will remain nearly constant for each simulation. Keeping the length of the heat exchanger at one meter, the sCO_2

convection coefficient can be plotted against Reynolds number for different particle channel thicknesses (See Figure 3.2). The sCO_2 convection coefficient increases with the Reynolds number, which is expected because the flow becomes more turbulent at higher Reynolds numbers. Smaller channel thickness also causes a larger increase in the sCO_2 coefficient.

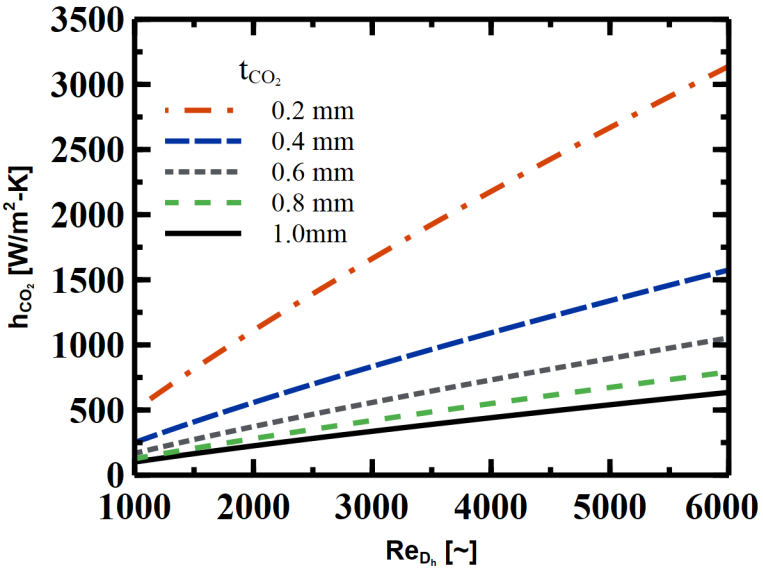

Figure 3.2 sCO2 convection coefficient as a function of Reynolds number and sCO2 channel thickness for a heat exchanger with L=1.

3.3.2 Particle Convection Coefficient

Using the Nusselt number relationship for the analytical solution of plug flow in a parallel plate moving packed bed heat exchanger from Muzychka et al. [62], the particle-wall convection is calculated.

$$\overline{Nu}_{Dh,H} = \frac{\bar{h}_{sw} D_h}{k_{s,eff}} = \left[\left(2 \frac{0.886}{\sqrt{Gz^{-1}}} \right)^{\frac{12}{5}} + 12^{\frac{12}{5}} \right]^{\frac{5}{12}} \tag{45}$$

where $D_{h,s}$ is the hydraulic diameter of the particle channel ($D_h = \frac{4t_s W}{2(t_s+W)} \approx 2t_s for\ W \gg t_S$), $k_{s,eff}$ is the effective bulk thermal conductivity of the solid, and Gz^{-1} is the inverse Graetz number ($Gz^{-1} = L/Pe_{Dh}D_h$). The inverse Graetz number is a function of the heat exchanger length (L), the Peclet number ($Pe_{D_h} = v_s D_h/\alpha_s$). Equation 45 is the Nusselt number with constant heat flux, which is used in this study because Watkins & Gould [16] and Albrecht & Ho [27] found good agreement with the correlation for circular and rectangular channels, respectively. The Nusselt number is only a function of the Graetz number, a non-dimensional number that is used to characterize transient heat conduction for laminar pipe flow [53]. Figure 3.3 demonstrates that the Nusselt number quickly reaches an asymptote of 12 as the inverse Graetz number increases. An effort should be made to keep the Graetz number low to increase the Nusselt number. Figure 3.4 shows how the average particle-wall convection coefficient is impacted by particle thermal conductivity and particle channel thickness assuming a thermally developed particle flow ($Gz^{-1} = 1$). The particle-wall convection coefficient increases with increasing thermal conductivity. This is expected because the convection coefficient is proportional to packed bed thermal conductivity. The particle-wall convection coefficient also increases with decreasing particle channel thickness. In general, the particle-wall convection coefficient will be less than the sCO_2 convection coefficient because packed bed thermal conductivity is fairly low for monodisperse packed beds. For example, Baumann & Zunft found that 600 μm bauxite particles had a thermal conductivity range of 0.22-0.54 (W/m-K) between ambient and 800 °C [14]. This shows the importance of using a binary particle distribution to increase packed bed thermal conductivity by reducing packed bed porosity.

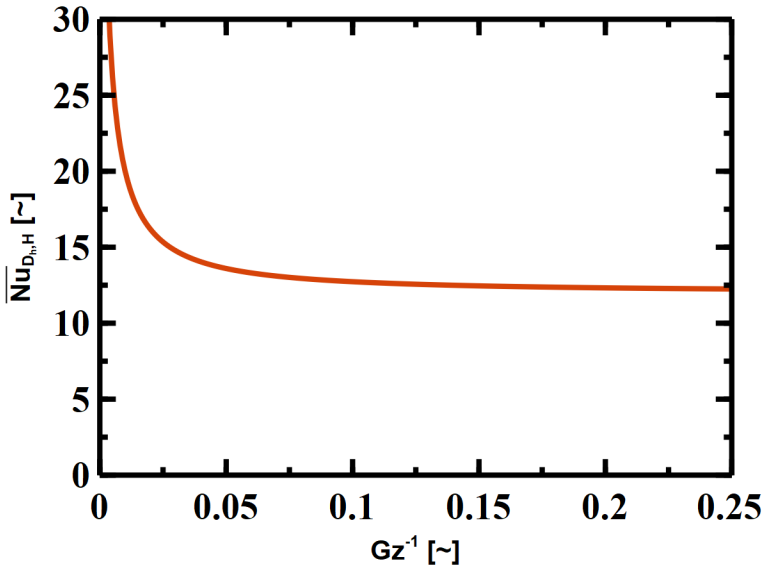

Figure 3.3 Average Nusselt number as a function of the inverse Graetz number for plug flow in a parallel plate heat exchanger.

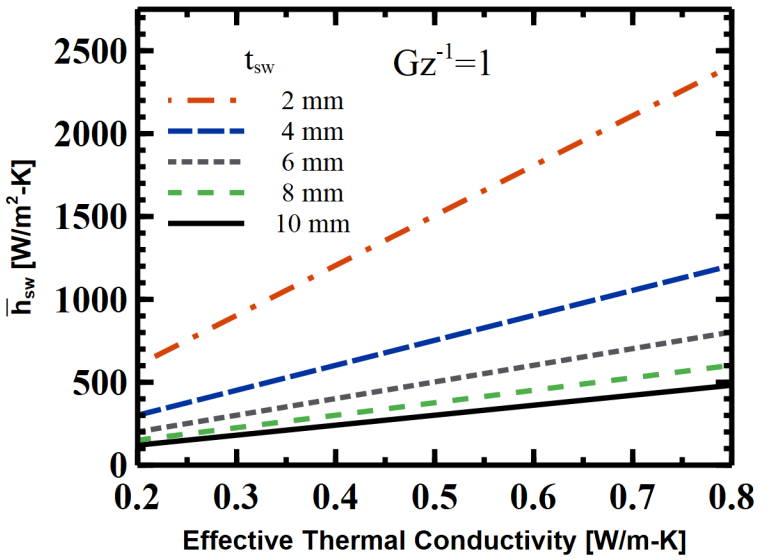

Figure 3.4 Average particle-wall convection coefficient as a function of packed bed thermal conductivity for different particle channel widths.

3.3.3 Particle-wall Contact Resistance

The particle-wall contact resistance is taken from Albrecht & Ho [26] and is defined as follows:

$$R_c^{"} = \frac{d_p}{2k_{s,eff}^{nw}} \tag{46}$$

where d_p is the Sauter mean diameter, $k_{s,eff}^{nw}$ is the near-wall particle thermal conductivity. When approaching the near-wall, the bulk packed bed thermal conductivity is no longer valid because there is a decrease in porosity in the near-wall region [47]. Denloye and Botterill determined that the near-wall porosity of monodisperse particle distribution can be calculated as follows:

$$\varepsilon_{nw} = \frac{(1-\varepsilon)(0.7293 + 0.5139Y)}{1+Y} \tag{47}$$

where ε is the bulk porosity and Y is defined as

$$Y = \frac{d_p}{2a} \tag{48}$$

The variable d_p is the Sauter mean diameter, and a is the radius of the heat transfer surface. For parallel flat plates, a is infinity. As a result, $Y = 0$ in this model. With the near-wall porosity, the thermal conductivity is calculated using the ZBS model. The use of an updated porosity at the near-wall to calculate the thermal conductivity is justified because CFD simulations using a radial porosity profile have shown good agreement with the ZS model [63]. While equation 47 was written for the porosity of monodisperse particle beds, this study will also use this correlation for binary particle mixtures.

Figure 3.5 demonstrates that lower near-wall packed bed thermal conductivity and larger particle sizes lead to a larger particle-wall contact resistance. Using a binary particle

distribution allows for a reduction in the bulk packed bed porosity; thus, the near-wall porosity and near-wall thermal conductivity will both be higher.

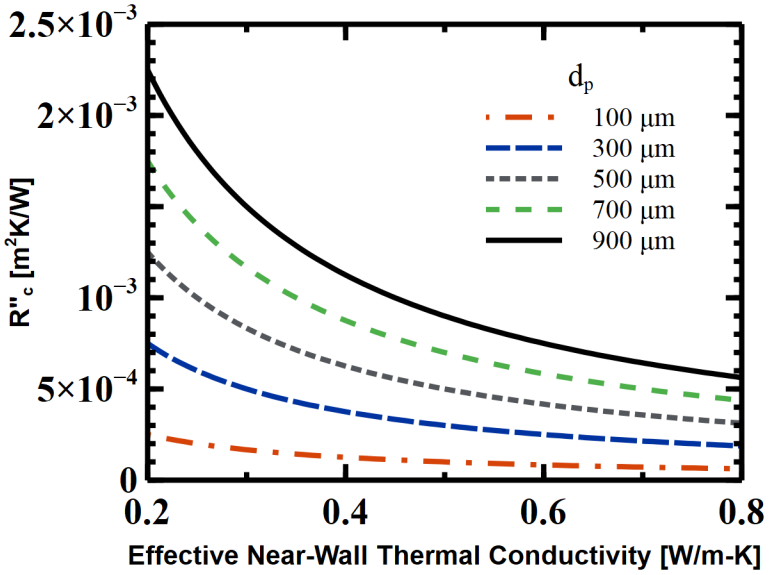

Figure 3.5 **Particle-wall contact resistance as a function of near-wall packed bed thermal conductivity for many particle diameters.**

3.4 Moving Packed Bed Heat Exchanger Modeling - Monodisperse Results

Before exploring binary mixtures in shell-and-plate moving packed bed heat exchangers, monodisperse particle systems are studied to clearly show the differences between the two approaches. This section will compare the results for a single-bank moving packed bed heat exchanger using the Yagi & Kuni without radiation thermal conductivity model (Equation 15), a model that has been used by Albrecht & Ho in the past [26], and the ZBS thermal conductivity model, a model that Albrecht & Ho recently started using [25]. The section will start by presenting the overall heat transfer coefficient results and will be followed by a description of what makes the results different and how a binary particle mixture could be used to improve shell-and-plate moving packed bed heat exchanger performance.

3.4.1 Overall Heat Transfer Coefficient

The moving packed bed heat exchanger model was run using all the parameters in Table 3.1. Both thermal conductivity models used the parameters in Table 2.2 except for the initial porosity which was set 0.4 because that is the standard porosity for a loosely packed bed of monodisperse particles [31]. Figure 3.6 shows the results for the overall heat transfer coefficient when using the Yagi & Kuni and the ZBS thermal conductivity models. The two models have starkly different results. Using the ZBS model, the overall heat transfer coefficient continually increases with particle size while the opposite is true for the Yagi & Kuni model. Looking at each resistance component shows why the results are so drastically different between the two models.

Simulation results using both models show that the Yagi & Kuni model leads to a higher resistance than the ZBS model for each particle size larger than 50 μm. The primary reason for the increase in thermal resistance from using the Yagi & Kuni model is a result of an increase in particle-wall contact resistance and sCO_2 convection resistance. The increase in particle-wall contact resistance is directly proportional to the increase in particle size because the packed bed thermal conductivity is constant in the Yagi & Kuni model (see Equation 15). The sCO_2 convection resistance increases because as the system has higher resistance, the particles must travel slower to achieve the same amount of heat transfer. The particle-wall convection resistance remains nearly constant for each particle size because the flow is thermally developed ($Gz^{-1} > 0.25$), the thermal conductivity is constant, and the channel properties are constant.

The ZBS model results demonstrate the importance of considering the temperature dependence of thermal conductivity. The particle-wall contact resistance for the 950 μm

particle decreased by 58% compared to the Yagi & Kuni model. As particle size increased, the sCO_2 mass flow rate increased causing a decrease in the sCO_2 convection resistance. The particle-wall convection resistance also decreases solely from an increase in thermal conductivity because the channel dimensions remained constant and the flow was thermally fully developed ($Gz^{-1} > 0.25$). As a result, the ZBS model will be used for calculating packed bed thermal conductivity for the rest of the thesis.

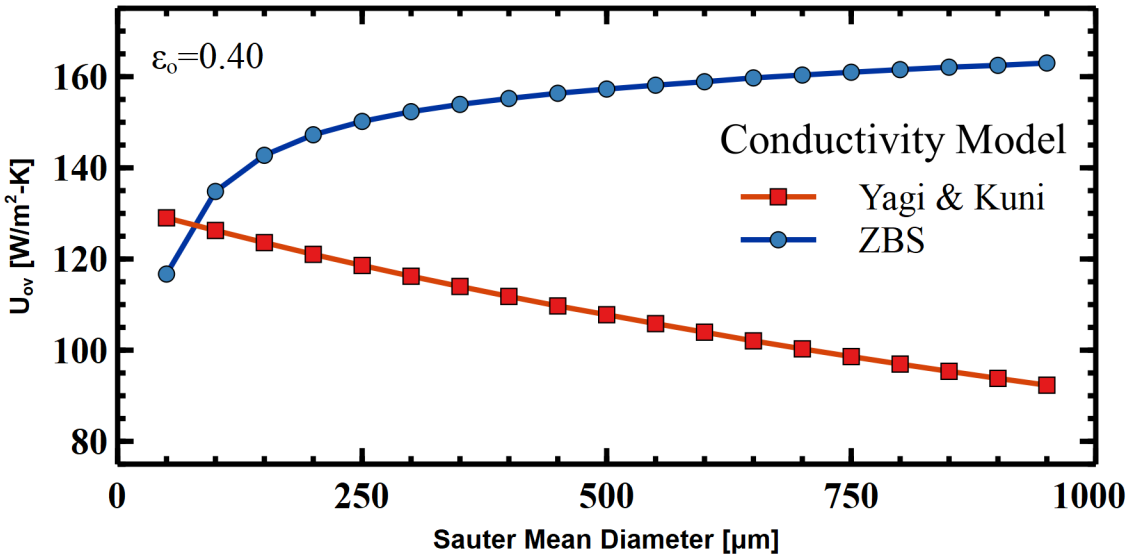

Figure 3.6 Overall heat transfer coefficient as a function of Sauter mean diameter when using the Yagi & Kuni and the ZBS thermal conductivity models.

3.4.2 Channel Thickness

While Figure 3.6 shows that larger particle sizes have higher overall heat transfer coefficients, particle channel thickness must also be considered. According to Albrecht & Ho, decreasing plate spacing can significantly improve the overall heat transfer coefficient [25]. However, a reduced channel thickness limits the particle size that can be used in the moving packed bed heat exchanger because particle channel thicknesses must be at least 10 particle diameters to achieve uniform and consistent flow [25]. Figure 3.7 shows the

results for overall heat transfer coefficient as a function of particle diameter for particle channel thicknesses of 3 – 12 mm for a single-bank moving packed bed heat exchanger. The results show the same trend as Albrecht & Ho for channel thickness; however, since sCO_2 pressure drop was not considered in this study, there is not a peak in the overall heat transfer coefficient before the maximum particle diameter as seen in Albrecht & Ho's study [25].

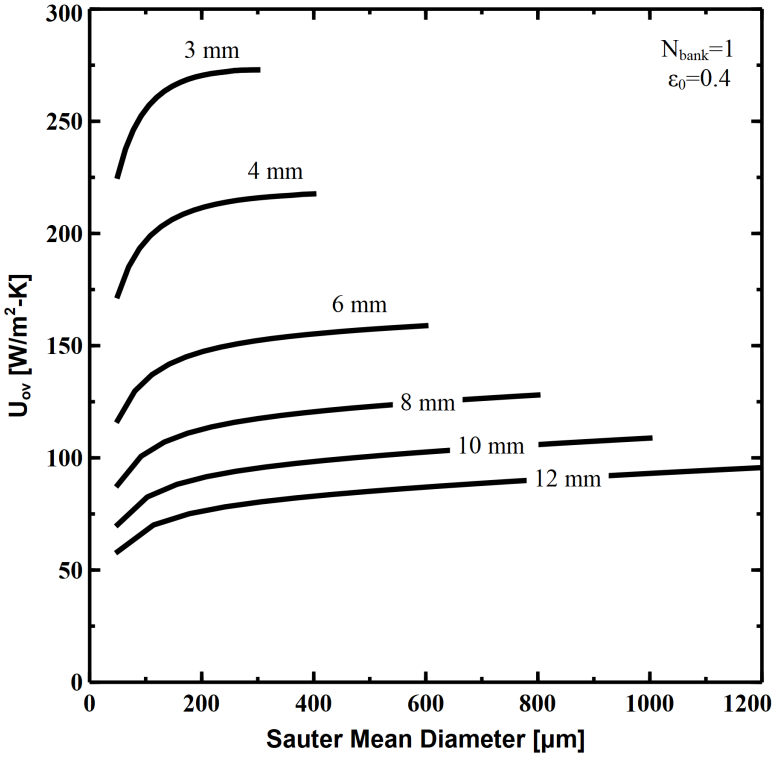

Figure 3.7 Overall heat transfer coefficient as a function of particle size and particle channel thickness for a single-bank moving packed bed heat exchanger. To meet flowability requirements, the particle channel thickness must be at least ten times larger than the largest particle in the channel.

While a smaller particle channel thickness provides larger overall heat transfer coefficients, utilizing a binary particle mixture can improve moving packed bed heat exchanger performance more by increasing the packed bed thermal conductivity. The next

section will show how binary particle mixtures of varying size ratios can improve the performance of moving packed bed heat exchangers.

3.5 Moving Packed Bed Heat Exchanger Modeling - Binary Results

Previous sections have shown that packed bed thermal conductivity can be increased by using a binary particle mixture. This section seeks to see if binary particle mixtures can increase the overall heat transfer coefficient in moving packed bed heat exchangers when compared to a monodisperse particle size. This section will start by analyzing how the overall heat transfer coefficient changes for the three particle mixtures tested in this study. Following that will be an analysis of how binary particle mixtures that meet particle segregation criteria can improve moving packed bed heat exchanger performance.

3.5.1 Overall Heat Transfer Coefficient

The moving packed bed heat exchanger model was run using all the parameters in Table 3.1. The ZBS model used the parameters outlined in Table 2.2. Figure 3.8A and Figure 3.8B show the overall heat transfer coefficient as a function of the large particle volume fraction and Sauter mean diameter, respectively, for the binary mixtures CP 16/30 – CP 70/140, CP 16/30 – CP 40/100, and HSP 16/30 – HSP 40/70 compared to monodisperse particles. The overall heat transfer coefficient has the same trend as the thermal conductivity results for a binary particle mixture. Initially, the overall heat transfer coefficient increases until the particle mixture reaches a minimum porosity and maximum packed bed thermal conductivity. The plot of overall heat transfer coefficient in Figure 3.8B is included so that particle channel thickness could be considered. For this simulation, all three particle mixtures have their highest overall heat transfer coefficients at Sauter

mean diameters that are at least ten times smaller than the particle channel thickness of 6 mm; therefore, the optimal particle mixture for each of the binary particle mixtures could be used in this heat exchanger configuration. In future simulations when particle channel thickness is changed, the Sauter mean diameter of the particle mixtures will need to be considered.

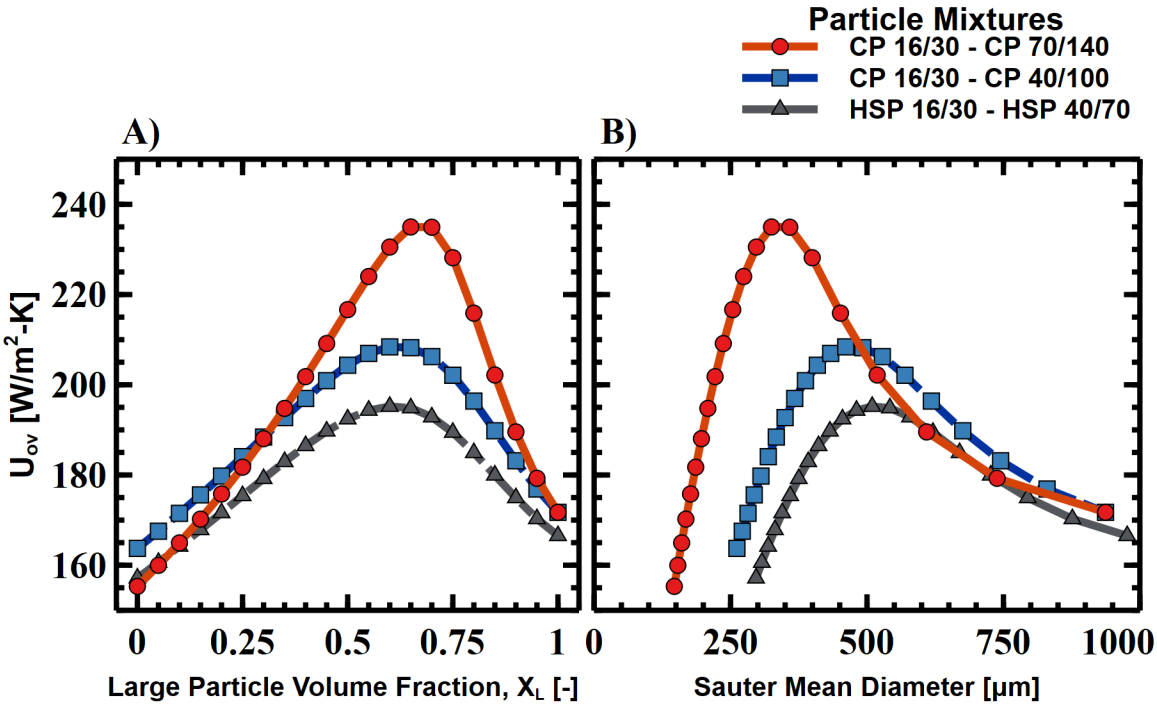

Figure 3.8 Overall heat transfer coefficient as a function of A) large particle volume fraction and B) Sauter mean diameter for a moving packed bed heat exchanger with dimensions shown in Table 3.1.

Figure 3.9 shows the simulation results in terms of a percent increase in the overall heat transfer coefficient. A >40% increase is seen in CP 16/30 – CP 70/140 (r = 0.157), and around a 20% increase is seen for both CP 16/30- CP 40/100 (r = 0.279) & HSP 16/30 – HSP 40/70 (r = 0.304). The primary reason for the increase the overall heat transfer coefficient is a result of the increase in packed bed thermal conductivity (see Figure 3.10).

Figure 3.11A and Figure 3.11B show each component of resistance as a function of the larger particle volume fraction and Sauter mean diameter, respectively, for CP 16/30 – CP 70/140. Both the particle and sCO_2 convection resistances are significantly lower than the monodisperse particle systems. Now that it has been established that binary particle mixtures can make a substantial difference in the overall heat transfer coefficient, a wider selection of particle size ratios that account for particle segregation criteria are considered.

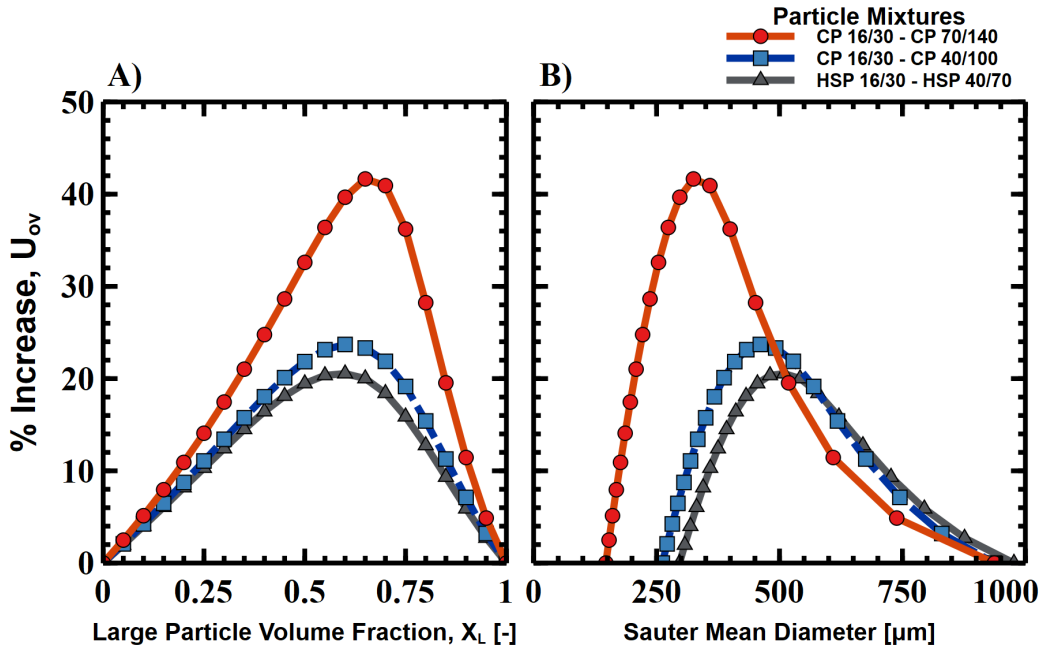

Figure 3.9 Percent increase in the overall heat transfer coefficient as a function of A) large particle volume fraction and B) Sauter mean diameter for a moving packed bed heat exchanger with dimensions shown in Table 3.1.

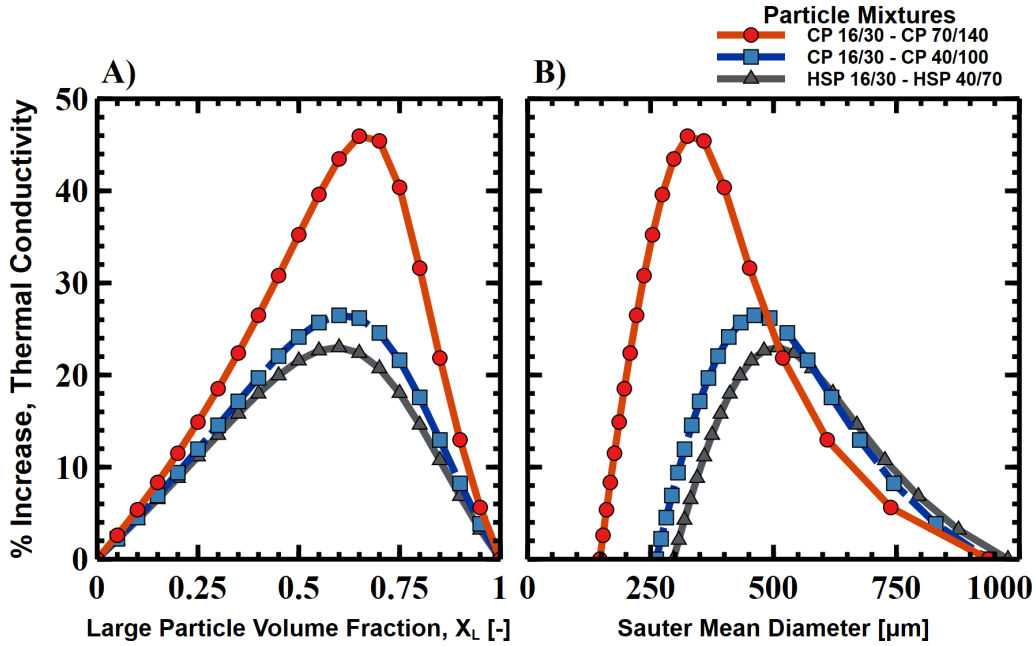

Figure 3.10 Percent increase in the packed bed thermal conductivity as a function of A) large particle volume fraction and B) Sauter mean diameter for a moving packed bed heat exchanger with dimensions shown in Table 3.1.

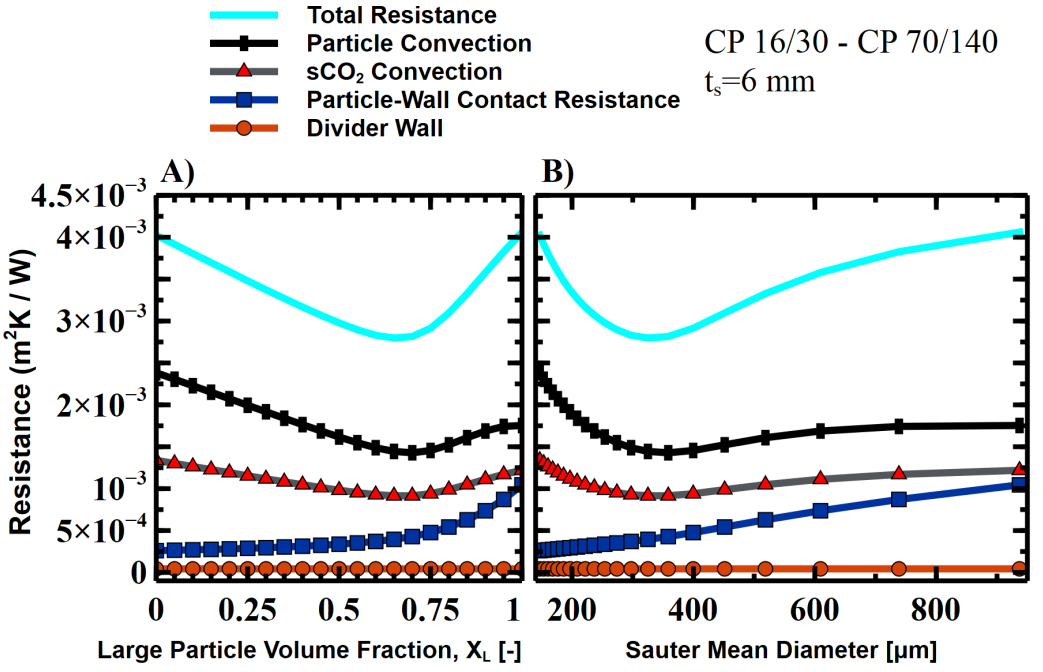

Figure 3.11 Resistance for CP 16/30 – CP 70/140 as a function of A) large particle volume fraction and B) Sauter mean diameter.

3.5.2 Size Ratio Impact

The previous section showed that size ratios below 0.304 lead to an increase in the overall heat transfer coefficient by 20% or more. This section will consider eight binary particle mixtures of CARBOBEAD CP products with size ratios from 0.157 - 0.810 (See Table 3.2) [39]. A wide range of particle mixtures are considered because particle sifting segregation becomes problematic if the following four conditions are present [64]:

1. A difference in particle size between the individual components, typically a minimum ratio of 2:1 or greater (a size ratio of 0.5 or smaller)
2. A sufficiently large mean particle size, typically one greater than approximately 500 μm
3. Free flowing material, and
4. Inter-particle motion

Each of the four conditions must be present in a mixture for segregation to occur [64]. Considering the particle segregation conditions, six binary mixtures of CARBOBEAD CP particles were simulated (See Figure 3.12). Three of the binary particle mixtures have a particle size ratio that is less than 0.5; however, the particles have Sauter mean diameters that are less than 500 μm. Figure 3.13 shows that these binary particle mixtures could experience up to a 23% increase in the overall heat transfer coefficient when compared to a monodisperse particle system. This result shows the large potential benefit of using a binary particle mixture into a moving packed bed heat exchanger; however, experimental studies of flowability should be conducted to ensure that binary mixtures will work in the thin particle channels. There is a potential that binary particle mixtures may require larger particle channel thicknesses, which are known to have worse overall heat transfer

coefficients, because binary particle mixtures have been shown to have worse flowability than monodisperse particle [65].

Table 3.2 Binary particle mixtures of each CARBOBEAD CP particle mixed with CP 70/140.

Binary Particle Mixture	Sauter Mean Diameter of Coarse Component (µm)	Sauter Mean Diameter of Fine Component (µm)	Size Ratio (~)
CP 16/30 - CP 70/140	937	147	0.157
CP 20/40 - CP 70/140	674		0.218
CP 30/60 - CP 70/140	459		0.320
CP 30/70 - CP 70/140	367		0.400
CP 40/70 - CP 70/140	327		0.449
CP 40/100 - CP 70/140	262		0.561
CP 40/140 - CP 70/140	223		0.660
CP 50/140 - CP 70/140	181		0.810

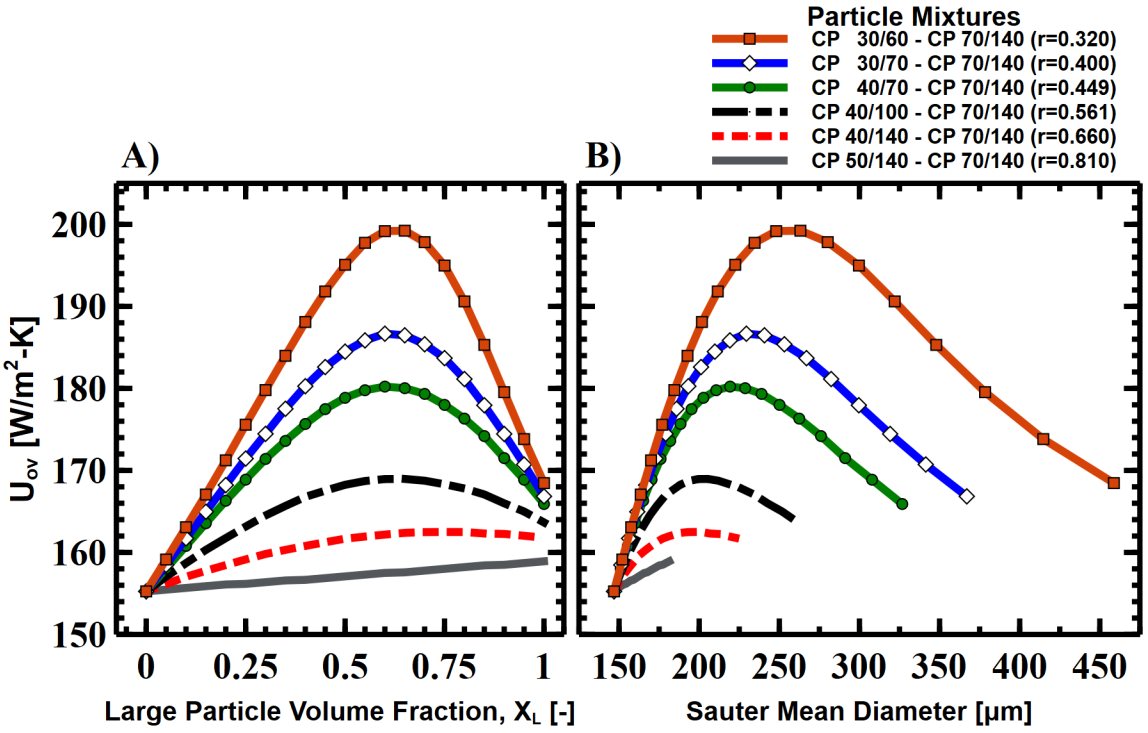

Figure 3.12 Overall heat transfer coefficient as a function of A) large particle volume fraction and B) Sauter mean diameter for multiple binary CARBOBEAD CP mixtures for a moving packed bed heat exchanger with dimensions shown in Table 3.1.

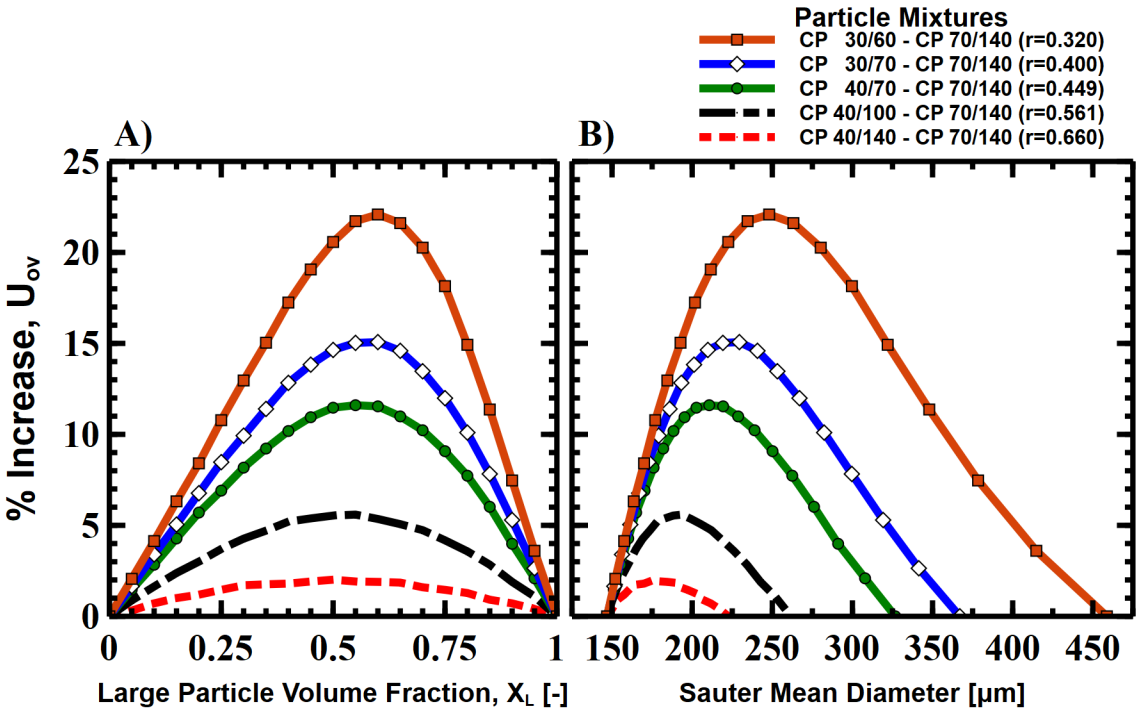

Figure 3.13 Percent increase in the overall heat transfer coefficient as a function of A) large particle volume fraction and B) Sauter mean diameter for multiple binary CARBOBEAD CP mixtures that meet particle segregation restrictions.

CHAPTER FOUR: CONCLUSION

This work suggests the use of binary particle mixtures in shell-and-plate moving packed bed heat exchanger as a way to increase the overall heat transfer coefficient by increasing the packed bed thermal conductivity. This is unique to previous studies because others have not considered using bimodal particle size distributions in moving packed bed heat exchangers.

Packed bed thermal conductivity and porosity models for binary particle mixtures across a range of large particle volume fractions and particle size ratios were presented. Using five ceramic particles with sizes between 100 - 1000 μm, nine unique binary particle mixtures were tested and compared to the presented models. Both the Standish and ZBS Models for porosity and thermal conductivity, respectively, were found to agree well with the collected experimental data taken up to 300 °C. The good agreement with the models presented warranted the models to be utilized in shell-and-plate moving packed bed heat exchanger modeling.

Evaluating the overall heat transfer coefficient for binary particle mixtures that meet sifting segregation requirements, the single-bank heat exchanger performance increases over 20% compared to a monodisperse particle system. As a result, this study demonstrates that binary particle mixtures should be considered as a potential option to improve the overall heat transfer coefficient in shell-and-plate moving packed bed heat exchangers.

CHAPTER FIVE: FUTURE WORK

While this study demonstrates that smaller size ratios lead to a greater decrease in porosity, future research should focus on what size ratio can be used in a practical system due to the risk of particle segregation for small size ratio mixtures. Future studies should also consider the flowability of particle systems with wide size distribution, especially at higher temperatures. Additionally, further studies could make improvements by measuring thermal conductivity using a transient hot-wire set-up similar to Baumann & Zunft so that thermal conductivity could be measured in the CSP operating temperature range [14].

REFERENCES

[1] NREL, “Concentrating Solar Power Projects,” 2019. [Online]. Available: https://solarpaces.nrel.gov/.

[2] S. S. Salvi *et al.*, “Technological advances to maximize solar collector energy output: A review,” *J. Electron. Packag. Trans. ASME*, vol. 140, no. 4, 2018.

[3] W. Fuqiang, C. Ziming, T. Jianyu, Y. Yuan, S. Yong, and L. Linhua, “Progress in concentrated solar power technology with parabolic trough collector system: A comprehensive review,” *Renew. Sustain. Energy Rev.*, vol. 79, no. May, pp. 1314–1328, 2017.

[4] C. T. Mark Mehos, J. Jorgenson, C. H. , Paul Denholm, and and K. Armijo, “Advancing Concentrating Solar Power Technology, Performance, and Dispatchability,” *Path To Sunshot*, no. 1, pp. 1–66, 2016.

[5] M. Mehos *et al.*, “Concentrating Solar Power Gen3 Demonstration Roadmap,” *Nrel/Tp-5500-67464*, no. January, pp. 1–140, 2017.

[6] T. Neises and C. Turchi, “Supercritical carbon dioxide power cycle design and configuration optimization to minimize levelized cost of energy of molten salt power towers operating at 650 °C,” *Sol. Energy*, vol. 181, no. November 2018, pp. 27–36, 2019.

[7] C. S. Turchi, J. Vidal, and M. Bauer, “Molten salt power towers operating at 600–650 °C: Salt selection and cost benefits,” *Sol. Energy*, vol. 164, no. November 2017, pp. 38–46, 2018.

[8] K. Wang, Y. L. He, and H. H. Zhu, “Integration between supercritical CO2 Brayton cycles and molten salt solar power towers: A review and a comprehensive comparison of different cycle layouts,” *Appl. Energy*, vol. 195, pp. 819–836, 2017.

[9] M. Sedighi, R. V. Padilla, R. A. Taylor, M. Lake, I. Izadgoshasb, and A. Rose, "High-temperature, point-focus, pressurised gas-phase solar receivers: A comprehensive review," *Energy Convers. Manag.*, vol. 185, no. November 2018, pp. 678–717, 2019.

[10] J. I. Linares, M. J. Montes, A. Cantizano, and C. Sánchez, "A novel supercritical CO2 recompression Brayton power cycle for power tower concentrating solar plants," *Appl. Energy*, vol. 263, no. October 2019, p. 114644, 2020.

[11] Y. Jiang, E. Liese, S. E. Zitney, and D. Bhattacharyya, "Design and dynamic modeling of printed circuit heat exchangers for supercritical carbon dioxide Brayton power cycles," *Appl. Energy*, vol. 231, no. September, pp. 1019–1032, 2018.

[12] J. Gifford, Z. Ma, and P. Davenport, "Thermal Analysis of Insulation Design for a Thermal Energy Storage Silo Containment for Long-Duration Electricity Storage," *Front. Energy Res.*, vol. 8, no. June, pp. 1–12, 2020.

[13] K. K. D. Repole and S. M. Jeter, "Design and analysis of a high temperature particulate hoist for proposed particle heating concentrator solar power systems," *ASME 2016 10th Int. Conf. Energy Sustain. ES 2016, collocated with ASME 2016 Power Conf. ASME 2016 14th Int. Conf. Fuel Cell Sci. Eng. Technol.*, vol. 1, pp. 1–10, 2016.

[14] T. Baumann and S. Zunft, "Properties of granular materials as heat transfer and storage medium in CSP application," *Sol. Energy Mater. Sol. Cells*, vol. 143, pp. 38–47, 2015.

[15] C. K. Ho, M. Carlson, K. J. Albrecht, Z. Ma, S. Jeter, and C. M. Nguyen, "Evaluation of Alternative Designs for a High Temperature Particle-to-sCO2 Heat Exchanger," *J. Sol. Energy Eng.*, vol. 141, no. 2, pp. 1–9, Apr. 2019.

[16] M. F. Watkins and R. D. Gould, "Heat Transfer to Vertical Dense Granular Flows at High Operating Temperatures," in *ASME 2017 11th International Conference on Energy Sustainability*, 2017.

[17] J. K. Spelt, C. E. Brennen, and R. H. Sabersky, "Heat Transfer to Flowing Granular Material," *Int. J. Heat Mass Transf.*, vol. 25, no. 6, pp. 791–796, 1982.

[18] J. S. Patton, R. H. Sabersky, and C. E. Brennen, “Convective heat transfer to rapidly flowing, granular materials,” *Int. J. Heat Mass Transf.*, vol. 29, no. 8, pp. 1263–1269, 1986.

[19] Z. Ma, G. Glatzmaier, and M. Mehos, “Fluidized bed technology for concentrating solar power with thermal energy storage,” *J. Sol. Energy Eng. Trans. ASME*, vol. 136, no. 3, pp. 1–9, 2014.

[20] J. C. Chen, J. R. Grace, and M. R. Golriz, “Heat transfer in fluidized beds: Design methods,” *Powder Technol.*, vol. 150, no. 2 SPEC. ISS., pp. 123–132, 2005.

[21] C. Geng, Y. Shao, W. Zhong, and X. Liu, “Thermodynamic Analysis of Supercritical CO2 Power Cycle with Fluidized Bed Coal Combustion,” *J. Combust.*, vol. 2018, 2018.

[22] Z. Ma and J. Martinek, “Fluidized-Bed Heat Transfer Modeling for the Development of Particle/Supercritical-CO2 Heat Exchanger,” in *ASME 2017 11th International Conference on Energy Sustainability*, 2017.

[23] T. Baumann and S. Zunft, “Development and Performance Assessment of a Moving Bed Heat Exchanger for Solar Central Receiver Power Plants,” *Energy Procedia*, vol. 69, no. 0, pp. 748–757, 2015.

[24] P. Bartsch, T. Baumann, and S. Zunft, “Granular Flow Field In Moving Bed Heat Exchangers : A Continuous Model Approach,” *Energy Procedia*, vol. 99, no. March, pp. 72–79, 2016.

[25] K. J. Albrecht and C. K. Ho, “Design and operating considerations for a shell-and-plate, moving packed-bed, particle-to-sCO 2 heat exchanger,” *Sol. Energy*, vol. 178, no. November 2018, pp. 331–340, 2019.

[26] K. J. Albrecht and C. K. Ho, “Heat Transfer Models of Moving Packed-Bed Particle-to-sCO2 Heat Exchangers,” *J. Sol. Energy Eng.*, vol. 141, no. 3, pp. 1–8, Jun. 2019.

[27] K. J. Albrecht and C. K. Ho, “High-temperature flow testing and heat transfer for a moving packed-bed particle/sCO2 heat exchanger,” *AIP Conf. Proc.*, vol. 2033, no. November, 2018.

[28] K. J. Albrecht, M. D. Carlson, H. F. Laubscher, R. Crandell, N. DeLovato, and C. K. Ho, "Testing and model validation of a prototype moving packed-bed particle-to-sCO2 heat exchanger," *Proc. 7Th Int. Conf. Electron. Devices, Syst. Appl.*, vol. 2306, no. December, p. 030002, 2020.

[29] M. Fernández-Torrijos, K. J. Albrecht, and C. K. Ho, "Dynamic modeling of a particle/supercritical CO2 heat exchanger for transient analysis and control," *Appl. Energy*, vol. 226, pp. 595–606, 2018.

[30] K. J. Albrecht and C. K. Ho, "Es2019-3893 Parametric Analysis of Particle Csp System Performance and Cost," pp. 1–11, 2019.

[31] H. Y. Sohn and C. Moreland, "The effect of particle size distribution on packing density," *Can. J. Chem. Eng.*, vol. 46, no. 3, pp. 162–167, Jun. 1968.

[32] R. Bauer and E. U. Schlünder, "Effective radial thermal conductivity of packings in gas flow. Part II. Thermal conductivity of the packing fraction without gas flow," *Int. Chem. Eng.*, vol. 18, no. 2, pp. 189–204, 1978.

[33] N. P. Siegel, M. D. Gross, and R. Coury, "The development of direct absorption and storage media for falling particle solar central receivers," *J. Sol. Energy Eng. Trans. ASME*, vol. 137, no. 4, pp. 1–7, 2015.

[34] E. Tsotsas and E.-U. Schlünder, "Impact of particle size dispersity on thermal conductivity of packed beds: Measurement, numerical simulation, prediction," *Chem. Eng. Technol.*, vol. 14, no. 6, pp. 421–427, Dec. 1991.

[35] R. Y. Yang, R. P. Zou, A. B. Yu, and D. Waals, "Computer simulation of the packing of fine particles," vol. 62, no. 3, pp. 3900–3908, 2000.

[36] A. B. Yu and N. Standish, "An analytical—parametric theory of the random packing of particles," *Powder Technol.*, vol. 55, no. 3, pp. 171–186, Jul. 1988.

[37] N. Siegel and G. Kolb, "Design and on-sun testing of a solid particle receiver prototype," *2008 Proc. 2nd Int. Conf. Energy Sustain. ES 2008*, vol. 2, pp. 329–334, 2009.

[38] J. Yin, Q. Zheng, and X. Zhang, “Heat transfer model of a particle energy storage-based moving packed bed heat exchanger,” *Energy Storage*, vol. 2, no. 1, pp. 1–14, 2020.

[39] CARBO, “CARBOBEAD Technical Data Sheet,” 2019. [Online]. Available: https://carboceramics.com/getmedia/f3f7794b-9cd4-4a8f-8184-93eb75f5bddd/CARBOBEAD-Technical-Data-Sheet-1001_317v5.pdf?ext=.pdf. [Accessed: 02-May-2021].

[40] A. B. Yu and N. Standish, “Porosity calculations of multi-component mixtures of spherical particles,” *Powder Technol.*, vol. 52, no. 3, pp. 233–241, Oct. 1987.

[41] A. O. O. Denloye and J. S. M. Botterill, “Heat transfer in flowing packed beds,” *Chem. Eng. Sci.*, vol. 32, no. 5, pp. 461–465, 1977.

[42] C. S. Chang and Y. Deng, “A nonlinear packing model for multi-sized particle mixtures,” *Powder Technol.*, vol. 336, pp. 449–464, Aug. 2018.

[43] S. Liu and Z. Ha, “Prediction of random packing limit for multimodal particle mixtures,” *Powder Technol.*, vol. 126, no. 3, pp. 283–296, Aug. 2002.

[44] M. C. Golob, “Convective Heat Transfer Performance of Sand for Thermal Energy Storage,” 2011.

[45] S. Yagi and D. Kunii, “Studies on Effective Thermal Conductivities in Packed Beds,” *Al*, vol. 3, no. 3, pp. 373–381, 1957.

[46] K. J. Albrecht and C. K. Ho, “Heat Transfer Models of Moving Packed-Bed Particle-to-sCO2 Heat Exchangers,” *J. Sol. Energy Eng. Trans. ASME*, vol. 141, no. 3, pp. 1–10, 2017.

[47] A. Denloye and J. Botterill, “A Theoretical Model of Heat Transfer to a packed or quiescent fluidized bed,” *Chem. Eng. Sci.*, vol. 33, no. 4, pp. 509–515, 1978.

[48] Z. Peng, E. Doroodchi, and B. Moghtaderi, “Heat transfer modelling in Discrete Element Method (DEM)-based simulations of thermal processes: Theory and model development,” *Prog. Energy Combust. Sci.*, vol. 79, p. 100847, Jul. 2020.

[49] M. Moscardini, Y. Gan, S. Pupeschi, and M. Kamlah, “Discrete element method for effective thermal conductivity of packed pebbles accounting for the Smoluchowski effect,” *Fusion Eng. Des.*, vol. 127, no. June 2017, pp. 192–201, Feb. 2018.

[50] Y. Qian, Z. Han, J.-H. Zhan, X. Liu, and G. Xu, “Comparative evaluation of heat conduction and radiation models for CFD simulation of heat transfer in packed beds,” *Int. J. Heat Mass Transf.*, vol. 127, pp. 573–584, Dec. 2018.

[51] R. K. McGEARY, “Mechanical Packing of Spherical Particles,” *J. Am. Ceram. Soc.*, vol. 44, no. 10, pp. 513–522, Oct. 1961.

[52] W. Van Antwerpen, C. G. Du Toit, and P. G. Rousseau, “A review of correlations to model the packing structure and effective thermal conductivity in packed beds of mono-sized spherical particles,” *Nucl. Eng. Des.*, vol. 240, no. 7, pp. 1803–1818, 2010.

[53] J. P. Holman, *Heat Transfer*, 10th ed. New York: McGaw-Hill, 2010.

[54] C. T. Hsu, P. Cheng, and K. W. Hong, “Modified Zehner-Schlunder Models for Stagnant Thermal Conductivity of Porous Media,” *Int. J. Heat Mass Transf.*, vol. 37, no. 17, pp. 2751–2759, 1994.

[55] S. Song and M. M. Yovanovich, “Correlation of Thermal Accommodation Coefficient for ‘Engineering’ Surfaces.,” *Am. Soc. Mech. Eng. Heat Transf. Div. HTD*, vol. 69, no. March, pp. 107–116, 1987.

[56] D. J. Falcioni, “Modeling of Heat Transfer in a Moving Packed Bed : Case of the Preheater in Nickel,” vol. 73, no. January, 2006.

[57] I. El and S. I. L. Park, “Performance analysis of a moving-bed exchanger in vertical pipes,” vol. 2, no. 0, pp. 911–918, 1996.

[58] C. Murphy *et al.*, “The Potential Role of Concentrating Solar Power within the Context of DOE’s 2030 Solar Cost Targets,” *NREL Tech. Rep. - NREL/TP-6A20-71912*, no. NREL/TP-6A20-71912, p. 137, 2019.

[59] V. Vesovic, W. A. Wakeham, G. A. Olchowy, J. V. Sengers, J. T. R. Watson, and J. Millat, “The Transport Properties of Carbon Dioxide,” *J. Phys. Chem. Ref. Data*, vol. 19, no. 3, pp. 763–808, Oct. 1990.

[60] R. Span and W. Wagner, “A New Equation of State for Carbon Dioxide Covering the Fluid Region from the Triple-Point Temperature to 1100 K at Pressures up to 800 MPa,” *J. Phys. Chem. Ref. Data*, vol. 25, no. 6, pp. 1509–1596, Nov. 1996.

[61] V. Gnielinski, “New Equations for Heat and Mass Transfer in Turbulent Pipe and Channel Flow,” *Int. Chem. Eng.*, vol. 16, no. 2, pp. 359–367, 1976.

[62] Y. S. Muzychka, E. Walsh, and P. Walsh, “Simple models for laminar thermally developing slug flow in non-circular ducts and channels,” *ASME Int. Mech. Eng. Congr. Expo. Proc.*, vol. 9, no. PART C, pp. 1867–1878, 2010.

[63] A. G. Dixon, A. K. Gurnon, M. Nijemeisland, and E. H. Stitt, “CFD testing of the pointwise use of the Zehner-Schlünder formulas for fixed-bed stagnant thermal conductivity,” *Int. Commun. Heat Mass Transf.*, vol. 42, pp. 1–4, 2013.

[64] G. Mehos, *Storage and Handling of Bulk Solids*. 2020.

[65] Y. Takeuchi *et al.*, “Characterization of mannitol granules and powder: A comparative study using two flowability testers,” *Int. J. Pharm.*, vol. 547, no. 1–2, pp. 106–113, 2018.

APPENDIX A

Particle Size Distributions

The particle distribtions for CP 16/30, CP 40/100, CP 70/140, HSP 16/30, and HSP 40/70 were taken from [39] or provided by Carbo during the purchase of the particles. The particle distributions for the binary particle distributions were calculated as follows:

$$Q_{i,binary} = X_L Q_{i,L} + (1 - X_L) Q_{i,s}$$

where $Q_{i,L}$ is the volume fraction of the coarse component, $Q_{i,s}$ is the volume fraction of the fine component, and X_L is the large particle volume fraction.

Table A.1 Particle size distribution as given by weight percentage retained by each sieve for each of the monodisperse and binary mixtures tested in this study.

Sieve Mesh Size (Microns)	8 - 12 (2360 - 1700)	12 - 16 (1700 - 1180)	16 - 20 (1180 - 850)	20 - 30 (850 - 600)	30 - 40 (600 - 425)	40 - 50 (425 - 300)	50 - 70 (300 - 212)	70 - 100 (212 - 149)	100 - 140 (149 - 105)	140 - 200 (105 - 74)
CP 16/30	0	3	74	23	0	0	0	0	0	0
CP 40/100	0	0	0	0	0	37	45	16	2	0
CP 70/140	0	0	0	0	0	0	1	51	43	5
HSP 16/30	0	3	85	12	0	0	0	0	0	0
HSP 40/70	0	0	0	0	0	48.1	51	0.8	0.1	0
CP 16/30 - CP 40/100 X_L=0.25	0	0.75	18.5	5.75	0	27.75	33.75	12	1.5	0
CP 16/30 - CP 40/100 X_L=0.50	0	1.5	37	11.5	0	18.5	22.5	8	1	0
CP 16/30 - CP 40/100 X_L=0.75	0	2.25	55.5	17.25	0	9.25	11.25	4	0.5	0
CP 16/30 - CP 70/140 X_L=0.25	0	0.75	18.5	5.75	0	0	0.75	38.25	32.25	3.75
CP 16/30 - CP 70/140 X_L=0.50	0	1.5	37	11.5	0	0	0.5	25.5	21.5	2.5
CP 16/30 - CP 70/140 X_L=0.75	0	2.25	55.5	17.25	0	0	0.25	12.75	10.75	1.25
HSP 16/30 - HSP 40/70 X_L=0.25	0	0.75	21.25	3	0	36.075	38.25	0.6	0.075	0
HSP 16/30 - HSP 40/70 X_L=0.50	0	1.5	42.5	6	0	24.05	25.5	0.4	0.05	0
HSP 16/30 - HSP 40/70 X_L=0.75	0	2.25	63.75	9	0	12.025	12.75	0.2	0.025	0

APPENDIX B

Experimental Porosity and Thermal Conductivity Results

Table B.1 Porosity measurements for each particle mixture compared to the model prediction.

Material	ε_{obs}	ε_{pred}	% Difference
HSP 40/70	0.384	0.382	0.64%
HSP 16/30 – HSP 40/70, X_L =0.25	0.335	0.352	5.14%
HSP 16/30 – HSP 40/70, X_L = 0.50	0.292	0.340	16.37%
HSP 16/30 – HSP 40/70, X_L = 0.75	0.300	0.350	16.47%
HSP 16/30	0.384	0.386	0.62%
CP 40/100	0.360	0.354	1.74%
CP 16/30 – CP 40/100, X_L = 0.25	0.310	0.313	1.18%
CP 16/30 – CP 40/100, X_L = 0.50	0.264	0.296	12.14%
CP 16/30 – CP 40/100, X_L = 0.75	0.268	0.318	18.62%
CP 16/30	0.360	0.356	1.18%
CP 70/140	0.360	0.370	2.77%
CP 16/30 – CP 70/140, X_L = 0.25	0.301	0.318	5.88%
CP 16/30 – CP 70/140, X_L = 0.50	0.235	0.284	20.94%
CP 16/30 – CP 70/140, X_L = 0.75	0.216	0.301	39.33%
CP 16/30	0.360	0.356	1.18%

All the monodisperse particles and binary particle mixtures were tested using the unattended measurement mode on the TEMPOS at temperatures of 25, 100, and 150 °C with the following test parameters: Mode: Conductivity/Resistivity, Sensor: TR-3, Power Mode: High (~3.6W), Read Time: One Minute (30 seconds heating and 30 seconds cooling), Interval Time: 15 min.

For both particle samples tested on the Thermtest, the following test parameters were used: Test Power: 0.1W, Test Time: 20 seconds, Calculations Window: 50 to 200 points, Sensor: HTK 5501 F1.

Table B.2 Thermal conductivity results for HSP 16/30 – HSP 40/70 for each temperature and particle mixture.

Material	Temperature [°C]	$k_{eff,obs}$ [W/m-K]	$k_{eff,pred}$ [W/m-K]	% Difference
HSP 40/70		0.230	0.255	10.03%
HSP 16/30 – HSP 40/70, X_L = 0.25		0.243	0.298	18.44%
HSP 16/30 – HSP 40/70, X_L = 0.50	25	0.297	0.343	13.39%
HSP 16/30 – HSP 40/70, X_L = 0.75		0.294	0.337	12.77%
HSP 16/30		0.225	0.264	14.78%
HSP 40/70		0.281	0.278	1.06%
HSP 16/30 – HSP 40/70, X_L = 0.25		0.301	0.324	7.15%
HSP 16/30 – HSP 40/70, X_L = 0.50	100	0.318	0.372	14.54%
HSP 16/30 – HSP 40/70, X_L = 0.75		0.336	0.367	8.41%
HSP 16/30		0.278	0.291	4.46%
HSP 40/70		0.302	0.292	3.25%
HSP 16/30 – HSP 40/70, X_L = 0.25		0.313	0.340	7.98%
HSP 16/30 – HSP 40/70, X_L = 0.50	150	0.383	0.390	1.73%
HSP 16/30 – HSP 40/70, X_L = 0.75		0.369	0.385	4.28%
HSP 16/30		0.327	0.309	5.87%

Table B.3 Thermal conductivity results for CP 16/30 – CP 40/100 for each temperature and particle mixture.

Material	Temperature [°C]	$k_{eff,obs}$ [W/m-K]	$k_{eff,pred}$ [W/m-K]	% Difference
CP 40/100	25	0.211	0.274	23.08%
CP 16/30 – CP 40/100, X_L = 0.25		0.237	0.322	26.50%
CP 16/30 – CP 40/100, X_L = 0.50		0.285	0.376	24.19%
CP 16/30 – CP 40/100, X_L = 0.75		0.270	0.374	27.75%
CP 16/30		0.235	0.283	17.13%
CP 40/100	100	0.242	0.296	18.24%
CP 16/30 – CP 40/100, X_L = 0.25		0.312	0.348	10.12%
CP 16/30 – CP 40/100, X_L = 0.50		0.324	0.405	20.09%
CP 16/30 – CP 40/100, X_L = 0.75		0.331	0.405	18.24%
CP 16/30		0.283	0.311	9.00%
CP 40/100	150	0.281	0.311	9.64%
CP 16/30 – CP 40/100, X_L = 0.25		0.321	0.364	11.90%
CP 16/30 – CP 40/100, X_L = 0.50		0.335	0.424	20.95%
CP 16/30 – CP 40/100, X_L = 0.75		0.393	0.424	7.36%
CP 16/30		0.312	0.330	5.42%

Table B.4 Thermal conductivity results for CP 16/30 – CP 40/100 for each temperature and particle mixture. Asterisks (*) indicate that the measurement was taken using the Thermtest Hot Disk TPS 2500 S.

Material	Temperature [°C]	$k_{eff,obs}$ [W/m-K]	$k_{eff,pred}$ [W/m-K]	% Difference
CP 70/140	25	0.197	0.267	26.06%
CP 16/30 – CP 70/140, X_L = 0.25		0.255	0.324	21.36%
CP 16/30 – CP 70/140, X_L = 0.50		0.345	0.409	15.62%
CP 16/30 – CP 70/140, X_L = 0.75		0.341	0.444	23.17%
CP 16/30		0.235	0.283	17.13%
CP 70/140	100	0.214	0.287	25.56%
CP 16/30 – CP 70/140, X_L = 0.25		0.325	0.348	6.50%
CP 16/30 – CP 70/140, X_L = 0.50*		0.446	0.438	1.92%
CP 16/30 – CP 70/140, X_L = 0.50		0.399	0.438	8.98%
CP 16/30 – CP 70/140, X_L = 0.75		0.406	0.476	14.74%
CP 16/30*		0.340	0.311	9.47%
CP 16/30		0.283	0.311	9.00%
CP 70/140	150	0.257	0.300	14.24%
CP 16/30 – CP 70/140, X_L = 0.25		0.361	0.363	0.63%
CP 16/30 – CP 70/140, X_L = 0.50		0.394	0.456	13.47%
CP 16/30 – CP 70/140, X_L = 0.75		0.492	0.496	0.97%
CP 16/30		0.312	0.330	5.42%
CP 16/30 – CP 70/140, X_L = 0.50*	250	0.531	0.489	8.51%
CP 16/30*		0.426	0.368	15.68%
CP 16/30 – CP 70/140, X_L = 0.50*	300	0.533	0.505	5.63%
CP 16/30*		0.454	0.388	17.03%